

**Predatory journals, paper mills, and fake publications.  
Animals highly adapted to the times**

**Performance of an artificial intelligence tool  
in percutaneous breast biopsies**

**Image fusion-guided liver ablation: an effective tool  
for ultrasound invisible lesions**

**Four-dimensional computed tomography for the detection of  
parathyroid adenomas: diagnostic accuracy and clinical applications**

**Diffusion-weighted imaging for the head-neck region and spinal cord:  
echo planar and non-echo planar imaging technique**

**Pedunculated focal nodular hyperplasia complicated by torsion:  
a very rare atypical presentation**

**Anomalous pulmonary venous drainage, mixed type:  
report of an uncommon case**

**A rare cause of basal ganglia and thalamic hyperintensities:  
infantile nephropathic cystinosis**



# A U S T R A L

## JOURNAL OF IMAGING

### REVISTA CHILENA DE RADIOLOGÍA

Indexed in: SciELO, Scopus, EMBASE, DOAJ, LATINDEX Catálogo 2.0, MIAR, Bibliovigilance, Dialnet

ISSN: 2810-6954 / e-ISSN: 2810-708X

VOLUME 32. ISSUE 2, APRIL-JUNE 2026

#### Editorial Board

##### Editor in Chief

**David Ladrón de Guevara Hernández**

*IRAM, Hospital San Juan de Dios, Universidad Diego Portales, Santiago de Chile, Chile*

##### Co-Editor

**Patricia Guzmán Falcón**

*Hospital San Juan de Dios, Universidad Diego Portales, Santiago, Chile*

##### National Editors

**Juan P. Cruz**

*Clínica Santa María e Instituto de Neurocirugía,  
Santiago, Chile*

**Nicolás Sánchez Domínguez**

*Clínica Alemana, Universidad del Desarrollo,  
Santiago, Chile*

**Carla Sáez Tapia**

*Hospital Clínico, Universidad de Chile,  
Santiago, Chile*

**Claudia Astudillo Abarca**

*Clínica Las Condes,  
Santiago, Chile*

**Jorge Contardo Pérez**

*Hospital Clínico, Universidad de Chile,  
Santiago, Chile*

**Carlos Toledo**

*Hospital las Higueras, Talcahuano,  
Bio Bio, Chile*

**Eduardo Bravo Rius**

*Hospital de niños Dr. Luis Calvo Mackenna,  
Santiago, Chile*

**Felipe Allende Nuñez**

*Universidad Mayor y Universidad de San Sebastián,  
Santiago, Chile*

**Felipe Zumaeta Valenzuela**

*Hospital Regional de Iquique,  
Iquique, Chile*

##### International Editors

**Sonia Bermúdez Muñoz**

*Hospital Universitario Fundación Santa Fe de Bogotá,  
Bogotá, Colombia*

**Janio Szklaruk**

*MD Anderson Cancer Center,  
Houston, TX, Estados Unidos*

**Marcel Koenigkam Santos**

*Hospital das Clínicas de Bauru,  
Universidad de São Paulo, São Paulo, Brasil*

**Araceli Cué Castro**

*Hospital General Dr. Enrique Cabrera,  
Ciudad de México, México*

**Cristina García Villar**

*Hospital Universitario Puerta del Mar de Cádiz,  
Cádiz, España*

##### Advisory Editorial Board

**Julieta Aránguiz Ramírez**

*Bioestadística e Investigación Biomédica,  
Universidad Diego Portales, Santiago, Chile*

**Rolando Cocio**

*Salud Pública, Clínica Alemana,  
Universidad del Desarrollo, Santiago, Chile*

**Pablo Del Río López**

*Protección Radiológica, Hospital Militar de Santiago,  
Universidad Mayor, Santiago, Chile*



**PERMANER**

[www.permayer.com](http://www.permayer.com)

[www.resochradi.com](http://www.resochradi.com)

## Predatory journals, paper mills, and fake publications. Animals highly adapted to the times

### *Revistas depredadoras, paper mills y publicaciones falsas. Animales muy bien adaptados a los tiempos*

David Ladrón de Guevara-Hernández 

Editor in Chief, Austral Journal of Imaging/Revista Chilena de Radiología, Santiago, Chile

Journals that masquerade as scientific publications, providing authors with false information primarily for profit, are called “predatory journals”. They typically lack an adequate peer-review system, which undermines the scientific validity of the articles, and offer open access to readers on the condition that the author pays for it.

Common characteristics of predatory journals include:

- They charge authors a fee to publish.
- They are open access.
- They lack a genuine peer-review editorial process, allowing them to publish papers quickly and efficiently.
- They present false information on their website about editorial processes that are not actually carried out, credit famous editors who are not actually part of the journal, or omit or hide initial information about the fee that will ultimately be charged to the author.
- Many of them send repeated emails inviting well-known authors to publish their articles in their journals, without mentioning details of fees or “article processing charges.”
- They are not listed in the DOAJ (*Directory of Open Access Journals*), NLM (*National Library of Medicine*) catalogue, COPE (*Committee on Publication Ethics*), or *SCImago Journal Rank* indexes.

An easy way to recognize these journals is to verify that they do not appear in the aforementioned indexes. Another way is to directly consult the now-discontinued “Beall’s list”<sup>1</sup> or other newer databases that have compiled nearly 3,000 publications that qualify in part or entirely as predatory<sup>2</sup>.

It is necessary to clarify that predatory practices are based on the primary objective of profit, regardless of the scientific quality of the product, and that the open access model is also used by reputable journals with appropriate editorial processes<sup>3</sup>.

Another form of fraud is the hijacking of scientific journals by setting up a parallel website that impersonates a legitimate, but not very well-known, journal, supplanting its identity to profit financially. These fake journals also often send mass email invitations to publish “in an indexed journal,” with a link to the fake platform. Emerging indexed journals, but without their own website or journal links, are especially at risk of this falsification/identity theft.

For the authors, publishing in these journals has the same meaning as publishing in a predatory journal; that is, their article will not undergo peer review, with the consequent lack of scientific validity. Furthermore, these types of journals may also host low-quality or outright fake articles.

#### Correspondence:

David Ladrón de Guevara-Hernández  
E-mail: humdavidhm@hotmail.com

Date of reception: 15-01-2026

Date of acceptance: 06-02-2026

DOI: 10.24875/AJI.M26000039

Available online: 28-04-2026

Austral J. Imaging. (Engl. ed.). 2026;32(2):59-61

[www.resochradi.com](http://www.resochradi.com)

2810-708X / © 2026 Sociedad Chilena de Radiología. Published by Permanyer. This is an open access article under the CC BY-NC-ND license (<https://creativecommons.org/licenses/by-nc-nd/4.0/>).

The industrial generation of papers containing false or fabricated information, known as *paper mills*, is an extreme that has been reached given the large sums of money involved in an industry valued at €1.4 billion<sup>4</sup>. These are organizations or companies providing “editorial services” that design, produce, and sell articles that imitate a legitimate research<sup>5</sup>, but contain false information, generally with excellently written texts, impeccable methodologies, and interesting results. Artificial intelligence has undoubtedly helped to sophisticate, streamline, and expand this industry. This type of fraud is especially harmful to scientific activity, particularly in the healthcare field, as it generates false information that can harm people. Fabricating data is the worst-case scenario in the realm of scientific fraud.

The success and explosive proliferation of all these forms of publishing fraud are explained by the intense pressure to publish that many scientists and researchers face in an environment governed by the “publish or perish” mentality, which can determine job security, project viability, and access to funding. They are also partly explained by the shortcomings of the conventional publishing system, which unduly restricts access

for both authors who want to publish –lengthy review processes, high rejection rates– and readers who want to access their work –exorbitant fees for access to each article–thus hindering the solution to the problem.

In addition to condemning all forms of publishing fraud, it is necessary to review and optimize the editorial procedures of journals with editorial committees and appropriate article review processes, so that they become more attractive and accessible to both authors and readers.

## References

1. Beall's list of potential predatory journals and publishers. (Consulted 29-01-2026.) Available from: <https://beallist.net/#update>
2. The predatory journal list. (Consulted 29-01-2026.) Available from: <https://www.predatoryjournals.org/the-list/journals%20>
3. Orduña-Malea E. Las revistas científicas falsas han llegado para quedarse. Aula Magna [Blog]; 2025. Available from: <https://cuedespyd.hypotheses.org/19959>
4. Sabel B. Paper mills: global knowledge contamination by industrial-style fake science publishing. (Consulted 29-01-2026.) Available from: <https://www.morressier.com/o/event/61c0a43adec9ce0013c988ff/article/61d3a5d04a84e7b4701d9885>
5. COPE (Committee on Publication Ethics). Systematic manipulation of the publishing process via ‘paper mills’. (Consulted 29-01-2026.) Available from: <https://publicationethics.org/topic-discussions/systematic-manipulation-publishing-process-paper-mills>

## Reviewers 2025

We take this opportunity to sincerely thank the following professionals who reviewed articles submitted to the Austral Journal of Imaging/Revista Chilena de Radiología during 2025.

List of reviewers for *Austral Journal of Imaging/Revista Chilena de Radiología* in 2025

Name	Surname	Medical center/institution	Country
David	Ladrón de Guevara Hernández	Hospital San Juan de Dios	Chile
Patricia	Guzmán	Hospital San Juan de Dios	Chile
Francisco	Garrido Cisterna	P. Universidad Católica de Chile - Red Salud UC-Christus	Chile
Julieta	Aránguiz	Universidad Diego Portales	Chile
Carla	Sáez	Hospital Clínico Universidad de Chile	Chile
Carlos	Toledo Riquelme	Hospital Guillermo Grant Benavente	Chile
Felipe	Zumaeta	Hospital Regional de Iquique	Chile
Felipe	Castillo Aravena	Toronto General Hospital	Canada
Juan Pablo	Cruz Quiroga	Hospital Clínico de la Pontificia Universidad Católica	Chile
Patricia	Arancibia	Hospital Digital	Chile
Lizbet	Pérez Marrero	Hospital de Niños Luis Calvo Mackenna	Chile
Nicolás	Sánchez	Clínica Alemana - Hospital Padre Hurtado	Chile
Cristina	García Villar	Hospital Universitario Puerta del Mar	Spain
Felipe	Allende Núñez	Universidad Mayor - Philips	Chile
Eduardo	Bravo Rius	Hospital de Niños Luis Calvo Mackenna	Chile
Alex	Wash	Clínica Las Condes	Chile
Rolando	Cocio Arcos	Clínica Alemana de Santiago, Hospital San Juan de Dios	Chile
Solange	Rivera Mercado	P. Universidad Católica de Chile - Red Salud UC-Christus	Chile
Pablo	Soffia Sánchez	Clínica Alemana	Chile
Jorge	Llanos Cáceres	Clínica Alemana	Chile
Jorge	Contardo	Hospital San Pablo de Coquimbo	Chile
María José	Diez Castellanos	Hospital San Juan de Dios	Chile
Marcelo	López Ramírez	Hospital Clínico de la Universidad de Chile	Chile
Claudia	Astudillo Abarca	Clínica Las Condes	Chile
Marcel	Koenigkam Santos	Universidade de São Paulo	Brazil
Jorge	Díaz	Hospital JJ Aguirre	Chile
Camila	de la Barra Escobar	Clínica Alemana de Santiago, Hospital Sótero del Río	Chile
Francisca	Norambuena	Hospital San Juan de Dios	Chile
Patricia	Bitar Hirmas	Clínica Las Condes	Chile
Sara	Muñoz Chiamil	Clínica Las Condes	Chile
Tamara	Palavecino Bustos	Hospital Clínico Universidad de Chile	Chile
Pablo	Maturana	Universidad Mayor	Chile
Valentina	San Martín	Hospital Sótero del Río y Hospital San Juan de Dios	Chile
Antonio	Peñailillo	Universidad Católica	Chile
Arnoldo	Riquelme Pérez	Pontificia Universidad Católica de Chile	Chile
Masao	Yamamoto Ramos	Hospital Regional del Río	Mexico
Leslie	Muñoz Silva	Hospital Clínico de la Universidad de Chile	Chile
Carlos	Riquelme Pizarro	Red Salud UC-Christus	Chile
Gonzalo	Miranda	Hospital José Joaquín Aguirre	Chile
Claudia	Hernández Marchant	Clínica Las Condes	Chile
Lukas	Karachon	Universidad Católica	Chile
Giancarlo	Schiappacasse Faundes	Clínica Alemana, Hospital Militar	Chile
Cristián	Jarry Trujillo	Pontificia Universidad Católica de Chile	Chile

## Performance of an artificial intelligence tool in percutaneous breast biopsies

### Rendimiento de una herramienta de inteligencia artificial en biopsias percutáneas de mama

Paulina Neira-Vallejos<sup>1\*</sup>, María C. Vial<sup>1</sup>, Carolina Behnke<sup>1</sup>, Marcelo Poblete-Becker<sup>1</sup>, M. Rosario van Wersch<sup>2</sup>, and Emilia Santelices<sup>2</sup>

<sup>1</sup>Radiology Department, Centro de la Mama de Clínica MEDS La Dehesa; <sup>2</sup>Faculty of Medicine, Universidad de Los Andes. Santiago, Chile

#### Abstract

**Introduction:** The use of artificial intelligence (AI) tools in breast ultrasound has shown an increase in the diagnostic accuracy of breast cancer. **Objective:** To evaluate the diagnostic performance of artificial intelligence (AI) software in the detection of breast cancer in breast lesions biopsied under ultrasound guidance. **Material and methods:** This prospective diagnostic testing study included the results of patients who underwent ultrasound-guided percutaneous breast biopsy. Images were analyzed and classified by degree of suspicion, first with an ACR BI-RADS category assigned by a specialist radiologist and then by AI software. These were subsequently correlated with the histopathology results obtained from the biopsy, which served as the reference standard. **Results:** 181 lesions were included in this study, of which 80 were malignant and 101 benign lesions. The sensitivity of the AI tool was 95%, specificity 58%, positive predictive value (PPV) 64%, negative predictive value (NPV) 93%, and accuracy 0.74. The values obtained by the radiologists were 98% sensitivity, 19% specificity, 49% PPV, 95% NPV, and 0.54 accuracy. **Conclusions:** The AI software demonstrated superior specificity and PPV compared to radiologists in lesions biopsied and could therefore be used to reduce the number of biopsies with benign results.

**Keywords:** Ultrasound. Breast. Core biopsy. Artificial intelligence.

#### Resumen

**Introducción:** El uso de herramientas de inteligencia artificial (IA) en ecografía mamaria ha mostrado un aumento en la exactitud diagnóstica del cáncer de mama. **Objetivo:** Evaluar el rendimiento diagnóstico de un software de inteligencia artificial (IA) en lesiones mamarias biopsiadas bajo guía ecográfica. **Material y métodos:** Estudio de pruebas diagnósticas prospectivo que incluyó los resultados de pacientes que concurren a realizarse una biopsia percutánea de mama bajo guía ecográfica y cuyas imágenes fueron analizadas y clasificadas por grado de sospecha, en primer lugar con una categoría ACR BI-RADS asignada por un radiólogo especialista y después por un software de IA. Posteriormente se correlacionaron con los resultados de histopatología obtenidos en la biopsia, que fue el estándar de referencia. **Resultados:** Se incluyeron 181 lesiones, de las cuales 80 fueron malignas y 101 benignas. La sensibilidad de la herramienta de IA fue del 95%, la especificidad del 58%, el valor predictivo positivo (VPP) del 64%, el valor predictivo negativo (VPN) del 93% y la exactitud de 0,74. Los radiólogos obtuvieron una sensibilidad del 98%, una especificidad del 19%, un VPP del 49%, un VPN del 95% y una exactitud de 0,54. **Conclusiones:** La herramienta de IA demostró una especificidad y un VPP superiores en comparación con los radiólogos en lesiones a las que se hizo biopsia, por lo que podría ser utilizada para disminuir el número de biopsias con resultado benigno.

**Palabras clave:** Ultrasonido. Mama. Biopsia core. Inteligencia artificial.

#### \*Correspondence:

Paulina Neira-Vallejos  
E-mail: paulina.neira@meds.cl

Date of reception: 02-05-2025

Date of acceptance: 01-09-2025

DOI: 10.24875/AJI.25000031

Available online: 28-04-2026

Austral J. Imaging. (Engl. ed.). 2026;32(2):62-67

[www.resochradi.com](http://www.resochradi.com)

2810-708X / © 2025 Sociedad Chilena de Radiología. Published by Permanyer. This is an open access article under the CC BY-NC-ND license (<https://creativecommons.org/licenses/by-nc-nd/4.0/>).

## Introduction

Breast cancer is the leading cause of cancer-related mortality in women worldwide, making it highly relevant<sup>1</sup>.

Mammography screening, with a detection rate of 4.1 cancers per 1000, has enabled timely detection, impacting the reduction of mortality from this cause<sup>2,3</sup>. While mammography remains the gold standard for breast cancer detection, its performance is limited in approximately 40% of the female population due to dense breast tissue, which affects its sensitivity<sup>4</sup>. Ultrasound assessment, as a supplementary screening method, has reduced the masking of lesions in dense breasts, with cancer detection rates ranging from 2.1 to 2.7 per 1000<sup>5</sup>. However, the positive predictive value of biopsies obtained in lesions visible only with supplementary ultrasound is low, between 2% and 21%, leading to the search for methods that improve results in the diagnostic process<sup>6</sup>. The use of artificial intelligence (AI) tools in mammography screening can improve the initial diagnosis of breast cancer<sup>7</sup>. The use of these tools in breast ultrasound has also been investigated, showing an increase in the diagnostic accuracy of breast cancer and decreasing the interpretation variability<sup>8</sup>. In November 2021, the Food and Drug Administration approved the use of the KOIOS DS device, an AI program for evaluating lesions visible on breast ultrasound. This AI tool is called a “decision support” tool and uses deep learning methods with advanced AI algorithms. In practice, the radiologist selects two orthogonal images of the lesion and places a region of interest in the center of the lesion. The software then automatically draws a rectangle around the lesion, characterizes its shape and orientation, and provides a level of suspicion.

The primary objective of this study is to evaluate the diagnostic performance of an AI tool, and secondary objectives are to compare this performance with that of radiologists and to assess whether its use improves discrimination for biopsy in breast lesions detected by ultrasound.

## Material and methods

A prospective diagnostic testing study was conducted to evaluate the diagnostic performance of an AI tool. All consecutive patients, who underwent ultrasound-guided biopsy at the request of their attending physician between April 2023 and June 2024 at the breast center of a private healthcare institution, were included.

In most cases, the attending physician ordered the biopsy because the lesion had been classified as suspicious (BIRADS [*Breast Imaging-Reporting and Data System*] 4 or 5) on breast ultrasound, but also in some cases, it was requested for lesions classified as probably benign, either because they were palpable, for an increased risk of developing breast cancer, or at the patient's request.

Lesions with a known inflammatory pathology result and those with a known cancer result were excluded.

The radiologist who performed the procedure assigned a clinical ACR (American College of Radiology) BIRADS category to the lesion at the time of the percutaneous biopsy, and subsequently, once the clinical suspicion category was recorded, the AI tool was applied using the KOIOS DS program; all of this was done before the biopsy results were known.

The AI software used for this study was the 3.6 KOIOS DS BREAST version.

The KOIOS DS suspicion level classification is divided into benign, probably benign, suspicious, and malignant, and these correlate with the suspicion levels of the ACR-BIRADS 5<sup>th</sup> edition<sup>9</sup> classification in its ultrasound section as follows:

- ACR-BIRADS Category 2: level 2 benign for the software.
- ACR-BIRADS Category 3: level 3 probably benign for the software.
- ACR-BIRADS Category 4: levels 4A, 4B, and 4C suspicious for the software.
- ACR-BIRADS Category 5: levels 4C+ malignant for the software.

The ACR-BIRADS categories 1 and 6 correspond to no findings and a diagnosed malignant neoplasm, respectively, and are therefore not considered in the KOIOS software classification.

All of the biopsies were performed with a 14G needle, except for two that were performed with a 10G needle.

Five radiologists with 4 to 27 years of experience in breast imaging (average 16 years) participated in classifying the level of suspicion of the lesions. They used handheld ultrasound on a GE Logic E10s ultrasound system with a 4-20 MH linear transducer.

The patient's age and the size of the biopsied lesion were recorded, and once the biopsy was reported by the pathologist, the histological result, which was considered the reference standard, was recorded.

Confidentiality was protected through anonymization measures, and the study was approved by the ethics committee.

### Statistical analysis

The relationship existing between the biopsy result (reference standard) and the lesion classification by the software and by the traditional ACR-BIRADS method performed by the radiologist, both prior to the biopsy, was evaluated. The sensitivity, specificity, positive predictive value (PPV), negative predictive value (NPV), and the accuracy of both the AI tool and the radiologists was calculated to assess the diagnostic performance using a binary method (benign or suspicious): for the software, “benign” refers to the benign and probably benign classifications, and “suspicious” to the suspicious and malignant classifications; for the radiologists, “benign” refers to the ACR-BIRADS 2 and 3 classifications, and “suspicious” to the ACR-BIRADS 4 and 5 classifications.

A subgroup analysis was performed for the non-palpable lesion group. The percentage of biopsies that could have been avoided, had the AI software’s recommendation been followed, was also calculated.

### Results

191 consecutive cases were included, of which nine corresponded to acute and subacute inflammatory pathology, including seven granulomatous mastitis cases and two acute inflammatory processes, which were excluded because the software specifications indicate that it is not suitable for evaluating acute inflammatory pathology. One patient who had already been diagnosed with breast cancer by percutaneous biopsy was also excluded, and a repeat biopsy for marker evaluation was requested. Thus, 181 cases and 177 patients were ultimately included, as four patients had biopsies of more than one lesion.

The average age of the patients was 49 years (range: 18–89 years). The size of the biopsied lesions ranged from 4 to 60 mm, with an average of 18 mm. Of the 181 lesions, 98 were palpable. There were 80 malignant lesions, 19 high-risk lesions, and 82 benign lesions. The histological results of the biopsies are detailed in [table 1](#).

The suspicion categories for the biopsied lesions assigned by the radiologists and by the software are detailed in [tables 2](#) and [3](#).

The software classified 42/181 lesions as BIRADS 2, none of which were malignant. Seven of the 42 corresponded to high-risk lesions (two papillary lesions without atypia and five benign phyllodes tumors); the five

**Table 1.** Histological results of breast lesions studied by percutaneous ultrasound-guided biopsy

Type of lesion	n = 181
Malignant lesions	80
Infiltrating ductal carcinoma	60
Infiltrating lobular carcinoma	9
Ductal carcinoma <i>in situ</i>	3
Papillary carcinoma	5
Mucinous carcinoma	2
Tubular carcinoma	1
High risk lesions	19
Intraductal Papiloma	6
Radiated scar	2
Phyllodes tumor	6
Atypical papillary lesion	1
Atypical fibroelastotic lesion	2
Flat epithelial atypia	1
Atypical ductal hyperplasia	0
Atypical lobular hyperplasia	1
Benign lesions	82
Fibroadenoma	44
Stromal fibrosis	14
Fat necrosis	4
Chronic inflammatory process	5
Pseudoangiomatous stromal hyperplasia	2
Hamartoma	1
Lymphocytic mastitis	2
Other	10

phyllodes tumors were palpable and classified as BIRADS 4A by the radiologists.

21/181 lesions were classified by the software as BIRADS 3, of which 4/21 were malignant (one papillary carcinoma *in situ* and three invasive ductal carcinomas, two of these were grade 3 and one grade 2), measuring 36, 19, 30, and 32 mm respectively. These four lesions were classified as suspicious (BIRADS 4 or 5) by the radiologists.

Among the 21 lesions classified as BI-RADS 3 by the software, three were high-risk lesions (a papilloma, a flat epithelial atypia, and a phyllodes tumor), which were classified as suspicious by the radiologists ([Fig. 1](#)).

There were eight lesions classified as BI-RADS 3 by the radiologists and as BI-RADS 4 by the AI software, of which seven were benign, with no high-risk lesions, and one lesion (1/8) that was malignant (infiltrating ductal carcinoma, grade 3 differentiation), measuring 20 mm.

The sensitivity of the AI tool was 95%, the specificity 58%, the PPV 64%, the NPV 93%, and the accuracy 0.74. The sensitivity of the radiologists was 98% (with values per radiologist ranging from 96% to 100%), the specificity was 19% (ranging from 13% to 25%), the PPV was 49% (ranging from 35% to 56%), the NPV was

**Table 2.** Suspicion categories of biopsied lesions assigned by radiologists and by the artificial intelligence software

BIRADS radiologists	Benign	Malignant	No. by category	BIRADS software*	Benign	Malignant	No. by category
2	0	0	0	2	42	0	42
3	20	1	21	3	17	4	21
4	79	47	126	4	38	50	88
5	2	32	34	4c+	4	26	30
Total	-	-	181	-	-	-	181

\*KOIOS DS artificial intelligence software.  
 BIRADS 2: benign appearance; BIRADS 3: probably benign; BIRADS 4: suspicious for malignancy; BIRADS 5 or 4c+: highly suspicious for malignancy.

**Table 3.** Binary classification (benign or suspicious) of biopsied lesions assigned by the radiologists and by the artificial intelligence software

BIRADS radiologists	Benign	Malignant	No. by category	BIRADS software*	Benign	Malignant	No. by category
2 y 3	20	1	21	2 y 3	59	4	63
4 y 5	81	79	160	4 y 4c+	42	76	118

\*KOIOS DS artificial intelligence software.  
 BIRADS 2 and 3: benign; BIRADS 4 and 5 or 4c+: suspicious.

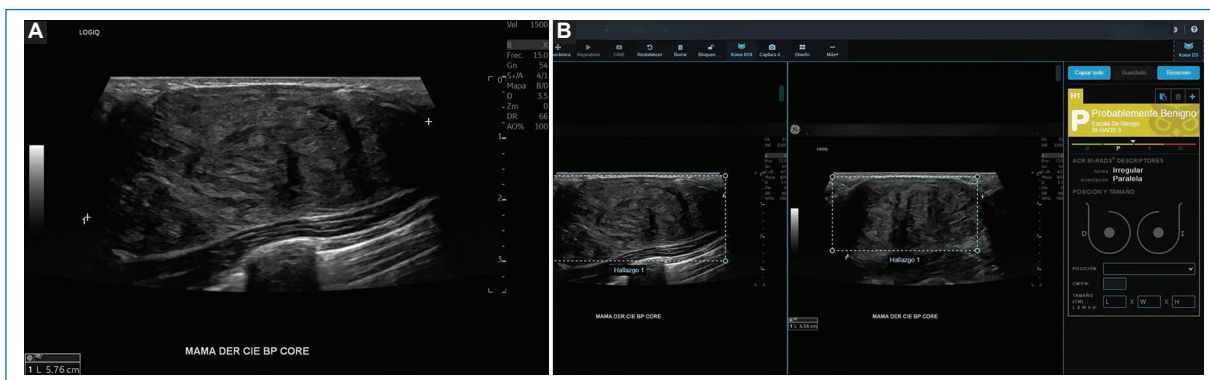


**Figure 1. A:** ultrasound performed by a radiologist who classified the nodule as BIRADS 4. **B:** classification by the artificial intelligence software of the same nodule as probably benign. The histological result of the core biopsy was: “histological findings consistent with a fibroepithelial lesion with areas of hypercellular stroma”. The patient was subsequently operated on, and the surgical biopsy revealed a “benign phyllodes tumor”.

95% (ranging from 75% to 100%), and the accuracy was 0.54 (ranging from 0.43 to 0.58).

In the subanalysis including only non-palpable lesions, AI had a sensitivity of 100%, a specificity of 47%, a PPV of 46%, a NPV of 100%, and an accuracy of 0.63, while for the radiologists the sensitivity was 100%, the specificity 24%, the PPV 41%, the NPV 100%, and the accuracy 0.50.

If biopsies had not been performed on the lesions categorized as benign and probably benign by the AI software, but classified as suspicious by radiologists (50/181), 27.6% of biopsies with benign results would have been avoided, and 2.2% of cancers would have been missed. If only biopsies had not been performed on lesions classified as benign (BIRADS 2) by the software and as suspicious by the radiologist (32/181),

17.7% of biopsies would have been avoided and no malignant lesion would have been missed.

## Discussion

Our results show a good performance by the AI tool in differentiating between benign and suspicious breast lesions visible on ultrasound, with a slightly lower sensitivity than radiologists, but with greater accuracy.

There are several publications that have generally shown good results with the use of these AI tools. The first, a retrospective study by Mango et al.<sup>8</sup>, included 900 breast lesions detected by 15 evaluators, and assessed the use of the KOIOS DS software as a decision support tool in the diagnosis of breast nodules from conventional ultrasound images, with a sensitivity of 98% for the software compared to 94% for the clinicians, and the software had a higher specificity (50% vs. 40%). In another retrospective study published by Berg et al.<sup>10</sup> in 2021, which included 319 patients and nine evaluators, the results showed a Receiver Operating Characteristic (ROC) curve for the software of 0.77, with no significant difference compared to that of the radiologists, which was 0.82.

There are studies that show that AI tools may be more useful for less experienced readers<sup>11,12</sup>. In the study by Park et al.<sup>11</sup>, less experienced radiologists significantly improved their NPV with AI assistance, while more experienced radiologists improved their PPV. In the study by Heller et al.<sup>12</sup>, there was no significant difference in accuracy, NPV, PPV, sensitivity, or specificity between radiologists and the AI software, but accuracy did improve, particularly for low-certainty lesions, improving the PPV (24.7% vs. 19.3%) and the specificity (57.8% vs. 44.6%).

A study with a population similar to ours is that of Browne et al.<sup>13</sup>, which included a total of 403 breast lesions or nodules that underwent percutaneous biopsy. The diagnostic performance of an AI tool and radiologists was evaluated, using the histological biopsy result as the reference point, and it was found that the number of benign biopsies performed on lesions classified by the software as BIRADS 3 had been significantly reduced, without failing to diagnose any malignant lesions.

In our study, there are 50 cases that the software categorized as BIRADS 2 or 3 and the radiologists classified as BIRADS 4 or 5. Of these 50 cases, 46 had benign results, and the other four turned out to be cancer and were classified as suspicious by the radiologists. If biopsies had not been performed on the lesions categorized as benign and probably benign by

the AI software, but classified as suspicious by radiologists, 27.6% of biopsies with benign results would have been avoided, but with a 2.2% loss of cancer diagnoses. If only the biopsies classified as BIRADS 2 by the software, and which were classified as suspicious by the radiologist, had not been performed, 17.7% of benign biopsies would have been avoided, and no malignant lesions would have been missed. This last result aligns with the findings of Guldogan et al.<sup>14</sup>, who described how the application of an AI tool would have avoided 11% of benign biopsies of lesions classified as BIRADS 2.

Our results clearly show the greater specificity and better PPV of the software compared to radiologists, which can be partly attributed to the fact that the radiologists classified a higher number of larger, primarily palpable, lesions as suspicious, while the software classified them as benign. As our sub-analysis of non-palpable lesions showed, the specificity of radiologists improves from 19% to 24% when palpable lesions are not considered. However, even taking this into account, none of the phyllodes tumors would have been diagnosed if the AI tool's classification had been followed, as they were categorized as BIRADS 2 and 3 by the software. All of them were palpable, and the radiologists categorized them as suspicious. This practice is explained by the fact that the ACR defines BIRADS category 3 only for non-palpable lesions. While the fact that a lesion is palpable is a clinical rather than a radiological criterion, radiologists generally choose to biopsy palpable lesions even if they appear benign on imaging<sup>15</sup>. Some authors question this approach, as it can lead to a significant number of false-positive results. In the series by Raza et al.<sup>16</sup>, the NPV of ultrasound in the evaluation of probably benign palpable nodules was high, at 99.4%, and therefore they conclude that follow-up is an acceptable alternative to biopsy, similar to the case of non-palpable nodules.

Among the limitations of our study is that the AI tool was used in a selected sample of patients with an indication for biopsy. Therefore, the results obtained regarding its performance are only applicable to similar populations and not to all women who undergo breast ultrasound for various indications. Another limitation is the small number of cases, which did not allow for further sub-analyses of the tool's performance, for example, regarding the molecular type of cancers.

## Conclusions

The application of an AI tool demonstrated good diagnostic performance in lesions that were biopsied, with

greater specificity and positive predictive value than the radiologists, so it could have a positive impact on clinical decision-making regarding performing biopsy, complementing the traditional radiological evaluation used to date, and with the potential to reduce false-positive biopsies.

## Funding

The authors declare that they have not received funding.

## Conflicts of interest

The authors declare no conflicts of interest.

## Ethical considerations

**Protection of human subjects and animals.** The authors declare that no experiments on humans or animals were performed for this research.

**Confidentiality, informed consent, and ethical approval.** The authors have followed their institution's confidentiality protocols, obtained informed consent from all patients, and secured approval from the Ethics Committee. SAGER guidelines have been followed as applicable to the nature of the study.

**Declaration on the use of artificial intelligence.** The authors declare that no generative artificial intelligence was used in the writing or creation of the content of this manuscript.

## References

- Sung H, Ferlay J, Siegel RL, Laversanne M, Soerjomataram I, Jemal A, et al. Global Cancer Statistics 2020: GLOBOCAN estimates of incidence and mortality worldwide for 36 cancers in 185 countries. *CA Cancer J Clin.* 2021;71:209-49. doi: 10.3322/caac.21660.
- Nelson HD, Fu R, Cantor A, Pappas M, Daeges M, Humphrey L. Effectiveness of breast cancer screening: systematic review and meta-analysis to update the 2009 US preventive services Task Force recommendation. *Ann Intern Med.* 2016;164:244-55.
- Sprague BL, Miglioretti DL, Lee CI, Perry H, Tosteson AAN, Kerlikowske K. New mammography screening performance metrics based on the entire screening episode. *Cancer.* 2020;126:3289-96. doi: 10.1002/cncr.32939.
- Mann RM, Athanasiou A, Baltzer PAT, Camps-Herrero J, Clauser P, Fallenberg EM, et al. European Society of Breast Imaging (EUSOBI). Breast cancer screening in women with extremely dense breasts recommendations of the European Society of Breast Imaging (EUSOBI). *Eur Radiol.* 2022;32:4036-45. doi: 10.1007/s00330-022-08617-6.
- Berg WA, Vourtsis A. Screening breast ultrasound using handheld or automated technique in women with dense breasts. *J Breast Imaging.* 2019;1:283-96.
- Hussein H, Abbas E, Keshavarzi S, Fazelzad R, Bukhanov K, Kulkarni S, et al. Supplemental breast cancer screening in women with dense breasts and negative mammography: a systematic review and meta-analysis. *Radiology.* 2023;306:e221785.
- Hernström V, Josefsson V, Sartor H, Schmidt D, Larsson AM, Hofvind S, et al. Screening performance and characteristics of breast cancer detected in the Mammography Screening with Artificial Intelligence trial (MASA): a randomised, controlled, parallel-group, non-inferiority, single-blinded, screening accuracy study. *Lancet Digit Health.* 2025;7:e175-83. doi: 10.1016/S2589-7500(24)00267-X.
- Mango VL, Sun M, Wynn RT, Ha R. Should we ignore, follow, or biopsy? Impact of artificial intelligence decision support on breast ultrasound lesion assessment. *Am J Roentgenol.* 2020;214:1445-52.
- Mendelson EB, Böhm-Vélez M, Berg WA, Whitman GJ, Feldman MI, Madjar H. ACR-BI-RADS ultrasound. En: *ACR BI-RADS Atlas: Breast Imaging Reporting and Data System.* Reston (VA): American College of Radiology; 2013.
- Berg WA, Gur D, Bandos AI, Nair B, Gizienski TA, Tyma CS, et al. Impact of original and artificially improved artificial intelligence-based computer-aided diagnosis on breast US interpretation. *J Breast Imaging.* 2021;3:301-11.
- Park YM, Kim EK, Lee JH, Ryu JH, Han SS, Choi SJ, et al. Palpable breast masses with probably benign morphology at sonography: can biopsy be deferred? *Acta Radiol.* 2008;49:1104-11.
- Heller SL, Wegener M, Babb JS, Gao Y. Can an artificial intelligence decision aid decrease false-positive breast biopsies? *Ultrasound Q.* 2021;37:10-5.
- Browne JL, Pascual MA, Pérez J, Salazar S, Valero B, Rodríguez I, et al. AI: can it make a difference to the predictive value of ultrasound breast biopsy? *Diagnostics (Basel).* 2023;13:811.
- Guldogan N, Taskin F, Icten GE, Yilmaz E, Turk EB, Erdemli S, et al. Artificial intelligence in BI-RADS categorization of breast lesions on ultrasound: can we omit excessive follow-ups and biopsies? *Acad Radiol.* 2024;31:2194-202. doi: 10.1016/j.acra.2023.11.031.
- Mahboubi-Fooladi Z, Sabahi M, Amin-Astani S, Khazaei M, Ghomi Z. Attitudes of practicing radiologists toward the management of palpable circumscribed breast masses. *J Breast Imaging.* 2023;5: 297-305.
- Raza S, Chikarmane SA, Neilsen SS, Zorn LM, Birdwell RL. BI-RADS 3, 4, and 5 lesions: value of US in management - follow-up and outcome. *Radiology.* 2008;248:773-81. doi: 10.1148/radiol.2483071786.

## Image fusion-guided liver ablation: an effective tool for ultrasound invisible lesions

### *Ablación hepática guiada por fusión de imágenes: una herramienta eficaz para lesiones no visibles en ultrasonido*

Benjamín Horwitz-Zanolli<sup>id</sup>, Nicolás Radic-González\*<sup>id</sup>, Antonio Vallejos-Cabezas<sup>id</sup>, Patricio Vargas-Hudson, Roberto Muñoz-Estrada, Paula Araneda-Castiglioni<sup>id</sup>, and Diego Constenla-Vásquez<sup>id</sup>

Imaging Department, Clínica Alemana, Universidad del Desarrollo, Santiago, Chile

#### Abstract

**Introduction:** Ultrasound (US)-guided percutaneous ablation is an effective alternative for the treatment of liver tumors. However, its utility decreases in small or isoechoic lesions. Image fusion allows for the localization of these lesions, increasing treatment possibilities and reducing the complication rate. **Objective:** To describe our center's experience with image fusion-guided liver tumor ablation and to assess its clinical utility and reproducibility. **Material and methods:** A retrospective study was conducted of image fusion-guided liver ablations performed between 2017 and 2023 at our center. A descriptive analysis was performed, including variables such as age, gender, tumor size and histology, visibility on US, technical success, local recurrence, and complications. **Results:** A total of 134 ablations were performed in 62 patients. Hepatocellular carcinomas accounted for 81% of cases, followed by metastases. 43% of the lesions were visible with US and 100% with image fusion. The technical success rate was 90% after the first session and 94% after a second session. The local recurrence rate was 12%. No serious complications were reported. **Conclusion:** Image fusion-guided liver ablation is a safe, effective, and useful technique, especially for the treatment of small lesions.

**Keywords:** Liver neoplasm. Image fusion. Ablation techniques. Interventional ultrasonography.

#### Resumen

**Introducción:** La ablación percutánea guiada por ultrasonido (US) es una alternativa eficaz en el tratamiento de tumores hepáticos. Sin embargo, su utilidad disminuye en lesiones pequeñas o isoecogénicas. La fusión de imágenes permite localizar estas lesiones, ampliando las posibilidades de tratamiento y reduciendo la tasa de complicaciones. **Objetivo:** Describir la experiencia en nuestro centro en la ablación de tumores hepáticos guiada por fusión de imágenes y evaluar su utilidad clínica y reproducibilidad. **Material y métodos:** Estudio retrospectivo de las ablaciones hepáticas guiadas por fusión de imágenes realizadas entre 2017-2023 en nuestro centro. Se realizó un análisis descriptivo de variables tales como edad, sexo, tamaño e histología tumoral, visibilidad en US, éxito técnico, recurrencia local y complicaciones. **Resultados:** Se realizaron 134 ablaciones en 62 pacientes. El 81% fueron hepatocarcinomas, seguidos por metástasis. El 43% de las lesiones fueron visibles con US y el 100% con fusión de imágenes. La tasa de éxito técnico fue del 90% tras la primera sesión y del 94% tras una segunda. La recurrencia local fue del 12%. No se reportaron complicaciones graves. **Conclusión:** La ablación hepática guiada por fusión de imágenes es una técnica segura, eficaz y útil, especialmente en el tratamiento de lesiones pequeñas.

**Palabras clave:** Neoplasia hepática. Fusión de imágenes. Técnicas de ablación. Ultrasonografía intervencionista.

#### \*Correspondence:

Nicolás Radic-González  
E-mail: nradicg@outlook.com

Date of reception: 30-04-2025

Date of acceptance: 01-09-2025

DOI: 10.24875/AJI.25000030

Available online: 28-04-2026

Austral J. Imaging. (Engl. ed.). 2026;32(2):68-72

[www.resochradi.com](http://www.resochradi.com)

2810-708X / © 2025 Sociedad Chilena de Radiología. Published by Permanyer. This is an open access article under the CC BY-NC-ND license (<https://creativecommons.org/licenses/by-nc-nd/4.0/>).

## Introduction

Ultrasound (US)-guided percutaneous ablation has emerged as an effective and minimally invasive alternative for the treatment of malignant liver tumors. However, the limited visualization of certain lesions has driven the development of new tools such as image fusion, which allow optimized lesion localization and therapeutic success. Percutaneous ablation involves the application of thermal energy by introducing a radiofrequency or microwave antenna directly into the lesion, which causes necrosis of the tumor tissue<sup>1,2</sup>. This is performed percutaneously under direct US visual guidance, as it is a widely available, low-cost tool and it does not emit ionizing radiation<sup>3</sup>. Nevertheless, this technique has several limitations, especially in the treatment of small and isoechoic lesions, which are difficult to visualize adequately with ultrasound<sup>4,5</sup>.

Ultrasound (US) fusion is an innovative technology that allows the localization of tumors not visible on ultrasound by combining US images with computed tomography (CT) or magnetic resonance imaging (MRI) studies, where the lesion is clearly identifiable. This has enabled the treatment of a greater number of tumors that were previously considered untreatable with conventional ablation methods, reporting similar technical success rates with a lower complication rate<sup>6,7</sup>. However, despite being a widely used technique in other countries, it remains a little-known tool in our setting, both among clinicians and radiologists, and there is limited literature on the subject in our country.

The objective of this study is to describe our center's experience with US fusion-guided liver ablation of malignant tumors, in order to evaluate its clinical utility and reproducibility, comparing our results with those reported in the international literature.

## Material and methods

A retrospective review was conducted, using the PACS (*Picture Archiving and Communication System*) imaging system of the Clínica Alemana de Santiago, of all the ultrasound image fusion-guided liver ablations performed between January 2017 and December 2023.

Patients who received combination therapies, such as percutaneous ablation combined with transarterial embolization, as well as those who underwent other procedures prior to ablation, were excluded from the sample. Also excluded were cases where control images were not available and where there was a loss of follow-up to patients after the procedure.

All of the procedures were performed after obtaining informed consent from the patient. Thermal ablation was performed by means of microwaves or radiofrequency, using 17G gauge antennas, applying a specific amount of energy for a defined period of time, according to the manufacturer's instructions based on the tumor size, aiming for an ablation margin of at least 5 mm peripheral to the lesion.

For the image fusion with ultrasound, contrast-enhanced CT or MRI studies in the arterial or venous phase with a maximum validity of three months from the date of the procedure, were used. A Canon Aplio i800 ultrasound scanner with Smart Fusion software and a system attached to the scanner was used, which, through the emission and reception of electromagnetic waves, allowed the dynamic synchronization of both modalities by moving the transducer (*Fig. 1*). *Figures 2* and *3* illustrate two cases where image fusion was used to locate tumors that were not visible on ultrasound.

The technical success of the procedure was defined as complete necrosis of the lesion at the first post-procedure imaging follow-up<sup>8</sup>. Local tumor recurrence was defined as the reappearance of the lesion at or near the ablation site after technical success at previous follow-up visits, using the LI-RADS (*Liver Imaging Reporting and Data System*) criteria for hepatocellular carcinoma (HCC) and the RECIST (*Response Evaluation Criteria in Solid Tumors*) criteria for other malignancies<sup>9</sup>. Complications were defined according to the classification system proposed by the Society of Interventional Radiology (SIR) USA, where they are classified as minor and major complications<sup>10</sup>.

Finally, a descriptive analysis of all these variables was performed, also including demographic variables such as patient gender and age, as well as lesion variables such as size and tumor histology. The number of lesions localizable during ablation using the conventional ultrasound method and the image fusion method was analyzed. Three groups were established according to tumor size (0-10, 10-20, and  $\geq 20$  mm) with the aim to evaluate ultrasound visibility in relation to lesion size.

## Results

A total of 134 liver ablations were performed on 62 patients (51% male), with an average age of 65 years. 81% of the lesions were HCC, followed in frequency by metastases from colon adenocarcinoma (*Table 1*). The average size of the treated lesions was 15 mm (*Fig. 4*).

Of the total lesions treated ( $n = 134$ ), only 43% ( $n = 58$ ) were visible by conventional ultrasound during

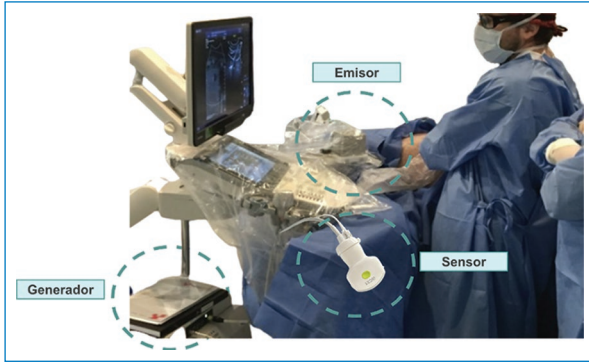


**Figure 1.** Representative image of the different components that make up the image fusion system attached to the ultrasound machine. The circles with dashed lines indicate its main elements: the electromagnetic wave generator, the emitter, and the sensor.

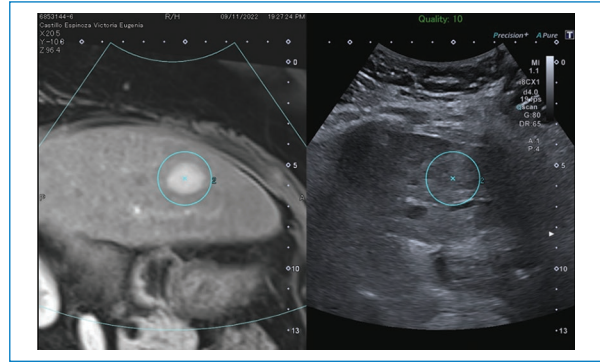


**Figure 3.** Image fusion between MRI and ultrasound prior to an HCC ablation. On the left, MRI showing an HCC. The image on the right shows the ultrasound, synchronized with the MRI, where the lesion is not visualized; however, the green ROI indicates its exact location. HCC: hepatocellular carcinoma; MRI: magnetic resonance imaging; ROI: region of interest.

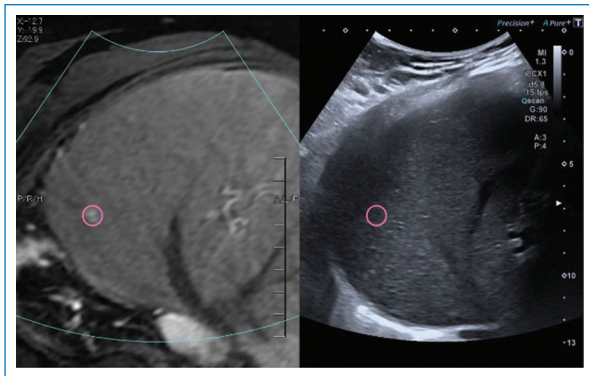


**Figure 2.** Synchronized images of an image fusion between MRI and ultrasound prior to the ablation of a small HCC (the pink ROI indicates the location of the lesion and the ablation margin to perform). On the left, the MRI shows a small hyperintense lesion, and on the right, the intraprocedural ultrasound where this lesion is not visible. HCC: hepatocellular carcinoma; MRI: magnetic resonance imaging; ROI: region of interest; US: ultrasound.

the procedure. **Table 2** shows the relationship between the size of the liver lesions, their visibility by conventional ultrasound and image fusion, and the technical success rate of the procedure. The technical success rate was approximately 90% after the first ablation session and 94% after a second session (**Fig. 5**). Local tumor recurrence was 12% after one year of follow-up.

No serious complications were reported according to the SIR classification system. A minor intraprocedural complication was reported, which consisted of a

**Table 1.** Tumor classification according to its histology

Type of tumor	Number of lesions ablated	%
Hepatocellular carcinoma	108	80.60
MTT from colon adenocarcinoma	11	8.21
MTT from melanoma	7	5.22
MTT from breast cancer	5	3.73
MTT from cholangiocarcinoma	1	0.75
MTT from adrenal carcinoma	1	0.75
MTT from submaxillary adenoid cystic carcinoma	1	0.75

MTT: metastasis.

transient hypertensive crisis, secondary to the ablation of an HCC that was in contiguity with the adrenal gland (**Fig. 6**), without requiring a transfer to a more complex unit or prolonging the patient's hospitalization time.

## Discussion

The use of image fusion techniques with ultrasound in the ablation of malignant liver tumors has increased significantly in recent years<sup>11,12</sup>. Its main usefulness has been described in the treatment of small and isoechoic lesions, as well as lesions located in complex anatomical sites with a poor ultrasound window due to their proximity to other structures such as the intestine or diaphragm<sup>13-15</sup>.

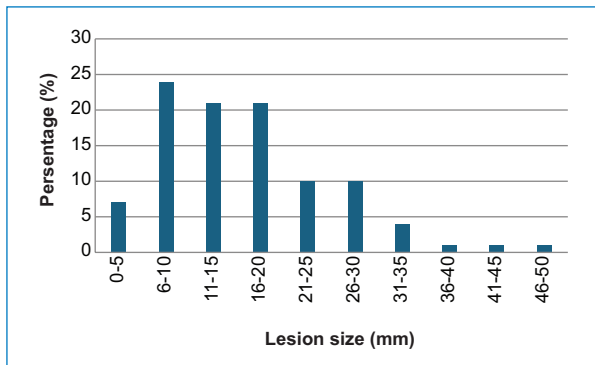


**Figure 4.** Percentage distribution of treated liver lesions according to size.

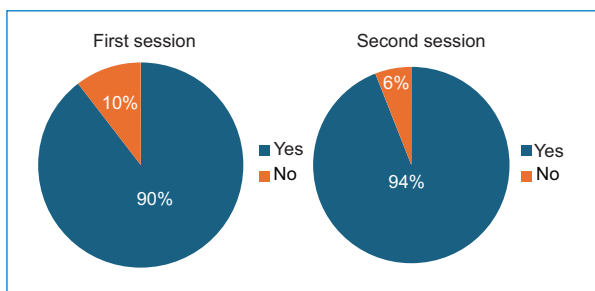


**Figure 5.** Percentage of technical success after the first and second ablation sessions.

In our study, only 43% of the treated lesions were localizable using conventional ultrasound. When stratified by size, it was shown that the group of smaller lesions (< 10 mm) had the lowest ultrasound visualization rate at only 7%, making image fusion essential for locating these lesions. Despite the low visibility with conventional ultrasound, all lesions could be treated using the ultrasound image fusion method, with a technical success rate of 90% in the first session and 94% in the second. These results are consistent with those reported in the literature, where it describes similar technical success rates, ranging between 84% and 94%<sup>4,7,16,17</sup>. It is worth noting that the technical success of the procedure was inversely proportional to the size of the treated lesions, being greater in the group of smaller lesions, with a rate close to 97%, while in the group of larger sized lesions (> 20 mm) it was approximately 62%. This could be explained by the greater technical difficulty that larger sized lesions present to achieve adequate ablation margins, often requiring the repetition of one or more ablation sessions to complete the treatment.

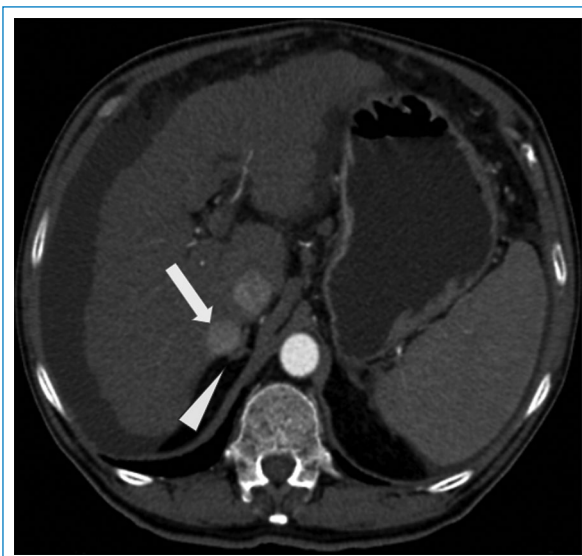


**Figure 6.** Abdominal computed tomography in the arterial phase, showing a hepatocellular carcinoma (arrow), contiguous to the right adrenal gland (arrowhead). A hypertensive crisis occurred during the thermal ablation procedure.

**Table 2.** Number of lesions visualized during the procedure with conventional ultrasound and with image fusion, and their technical success according to size

Size	Number of lesions	Visibility conventional ultrasound	Visibility US fusion	Technical success 1st session
< 10 mm	32	7%	100%	96.9%
10-20 mm	68	45%	100%	86.8%
> 20 mm	34	70%	100%	61.8%
Total	134	42.5%	100%	89.6%

On the other hand, image fusion has been shown not only to improve lesion visualization but also to decrease the rate of complications and local tumor recurrence. A recent meta-analysis published in 2023 compared conventional ultrasound-guided ablation with image fusion ablation, reporting a 30% reduction (relative risk [RR]: 0.70), 95% confidence interval ([95% CI]: 0.50-0.97, p=0.03) in the risk of complications, and a 39% reduction (RR: 0.61) in the risk of local recurrence in the group of patients in whom image fusion<sup>7</sup> was used. In our study, no serious complications were reported, and the local recurrence rate was 12%, however, since there was no control group, it is not possible to establish a comparison between the two techniques.

The main limitations of this study include its retrospective design, which may introduce bias in the collection of data. The statistical analysis was exploratory in nature, without a control group to allow comparison of both ablation techniques. Furthermore, a lengthy follow-up of patients was not achieved, which limits the assessment of long-term survival and the interpretation of the results. It is necessary to undertake prospective studies, with longer follow-up periods, to confirm these findings and more accurately evaluate the impact of this technique on long-term survival.

Finally, this study focused on one of the many technological innovations developed in recent years. It will be of particular interest for future research to explore the impact of other emerging tools, such as AI-assisted navigation systems and robotic devices, which also seek to improve the accuracy and effectiveness of minimally invasive procedures<sup>18,19</sup>.

## Conclusion

Percutaneous ablation of malignant liver tumors guided by ultrasound fusion imaging is a safe, reproducible, and clinically useful technique in our setting, especially for the treatment of small liver tumors. Its greater ability to locate lesions undetectable by conventional ultrasound allows for the treatment of a larger number of tumors with technical success rates similar to those reported in the international literature.

## Funding

The authors declare that they have not received funding.

## Conflicts of interest

The authors declare no conflicts of interest.

## Ethical considerations

**Protection of human subjects and animals.** The authors declare that the procedures followed were in accordance with the ethical standards of the responsible committee on human experimentation and with the World Medical Association and the Declaration of Helsinki. The procedures were authorized by the Institutional Ethics Committee.

**Confidentiality, informed consent, and ethical approval.** The authors have obtained approval from the Ethics Committee for the analysis of routinely collected

and anonymized clinical data; therefore, individual informed consent was not required. Relevant ethical recommendations have been followed.

### Declaration on the use of artificial intelligence.

The authors declare that no generative artificial intelligence was used in the writing or creation of the content of this manuscript.

## References

- Goldberg SN, Gazelle GS, Compton CC, Mueller PR, Tanabe KK. Treatment of intrahepatic malignancy with radiofrequency ablation: radiologic-pathologic correlation. *Cancer*. 2000;88(11):2452-63.
- Kim YS, Rhim H, Lim HK, Choi D, Lee MW, Park MJ. Coagulation necrosis induced by radiofrequency ablation in the liver: histopathologic and radiologic review of usual to extremely rare changes. *Radiographics*. 2011;31(2):377-90.
- Hotsen N, Puls R, Bechstein W, Felix R. Focal liver lesion tumors: Doppler ultrasound. *Eur Radiol*. 1999;9:428-35.
- De Muzio F, Cutolo C, Dell'Aversana F, Grassi F, Ravo L, Ferrante M, et al. Complications after thermal ablation of hepatocellular carcinoma and liver metastases: imaging findings. *Diagnostics (Basel)*. 2022;12(5):1151.
- Zou YW, Ren ZG, Sun Y, Wang Q, Liu J, Li X, et al. The latest research progress on minimally invasive treatments for hepatocellular carcinoma. *Hepatobiliary Pancreat Dis Int*. 2023;22:54-63.
- Mauri G, Cova L, De Beni S, Ierace T, Tondolo T, Cerri A, et al. Real-time US-CT/MRI image fusion for guidance of thermal ablation of liver tumors undetectable with US: results in 295 cases. *Cardiovasc Intervent Radiol*. 2015;38(1):143-51. doi: 10.1007/s00270-014-0897-y
- Sheng Y, Sun X, Sun H, Qi J, Li H, Luan J, et al. Fusion imaging versus ultrasound-guided percutaneous thermal ablation of liver cancer: a meta-analysis. *Acta Radiol*. 2023;64(9):2506-17.
- Shiina S, Sato K, Tateishi R, Shimizu M, Ohama H, Hatanaka T, et al. Percutaneous ablation for hepatocellular carcinoma: comparison of various ablation techniques and surgery. *Can J Gastroenterol Hepatol*. 2018;2018:4756147.
- Berber E, Siperstein A. Local recurrence after laparoscopic radiofrequency ablation of liver tumors: an analysis of 1032 tumors. *Ann Surg Oncol*. 2008;15(10):2757-64. doi: 10.1245/s10434-008-0043-7
- Crocetti L, de Baere T, Lencioni R. Quality improvement guidelines for radiofrequency ablation of liver tumours. *Cardiovasc Intervent Radiol*. 2010;33(1):11-7.
- Carriero S, Della-Pepa G, Monfardini L, Vitale R, Rossi D, Masperi A, et al. Role of fusion imaging in image-guided thermal ablations. *Diagnostics (Basel)*. 2021;11(3):549.
- Lee MW. Fusion imaging of real-time ultrasonography with CT or MRI for hepatic intervention. *Ultrasonography*. 2014;33(4):227-39. doi: 10.14366/usg.14021
- Ahn SJ, Lee JM, Lee DH, Lee SM, Yoon JH, Kim YJ, et al. Real-time US-CT/MR fusion imaging for percutaneous radiofrequency ablation of hepatocellular carcinoma. *J Hepatol*. 2017;66(2):347-54. doi: 10.1016/j.jhep.2016.09.003
- Venkatesan AM, Kadoury S, Abi-Jaoudeh N, Levy EB, MaassMoreno R, Krücker J, et al. Realtime FDG PET guidance during biopsies and radiofrequency ablation using multimodality fusion with electromagnetic navigation. *Radiology*. 2011;260(3):848-56.
- Calandri M, Mauri G, Yevich S, Gazzera C, Basile D, Gatti M, et al. Fusion imaging and virtual navigation to guide percutaneous thermal ablation of hepatocellular carcinoma: a review of the literature. *Cardiovasc Intervent Radiol*. 2019;42(5):639-47. doi: 10.1007/s00270-019-02167-z
- Xu ZF, Xie XY, Kuang M, Liu GJ, Chen LD, Zheng YL, et al. Percutaneous radiofrequency ablation of malignant liver tumors with ultrasound and CT fusion imaging guidance. *J Clin Ultrasound*. 2014;42(6):321-30. doi: 10.1002/jcu.22141
- Zensen S, Bucker A, Meetschen M, Haubold J, Opitz M, Theysohn JM, et al. Current use of percutaneous image-guided tumor ablation for the therapy of liver tumors: lessons learned from the registry of the German Society for Interventional Radiology and Minimally Invasive Therapy (DeGIR) 2018-2022. *Eur Radiol*. 2024;34(5):3322-30. doi: 10.1007/s00330-023-10412-w
- Lanza C, Carriero S, Buijs EFM, Mortellaro S, Pizzi C, Sciacqua LV, et al. Robotics in interventional radiology: review of current and future applications. *Technol Cancer Res Treat*. 2023;22:15330338231152084.
- Lesanier A, Khlaut J, Dancette C, Tselikas L, Bonnet B, Boeken T. Artificial intelligence in interventional radiology: current concepts and future trends. *Diagn Interv Imaging*. 2025;106(1):5-10. doi: 10.1016/j.diii.2024.08.004

## Four-dimensional computed tomography for the detection of parathyroid adenomas: diagnostic accuracy and clinical applications

### Tomografía computarizada de cuatro dimensiones para detección de adenomas paratiroides: precisión diagnóstica y aplicaciones clínicas

Rolando Cocío<sup>id</sup>, Daniela Barahona<sup>id</sup>, Joaquín Cristi\*<sup>id</sup>, and Fernanda Blaskovic<sup>id</sup>

Imaging Department, Faculty of Medicine, Clínica Alemana – Universidad del Desarrollo, Santiago, Chile

#### Abstract

Primary hyperparathyroidism is diagnosed based on laboratory abnormalities and in up to 80% of cases it is caused by a solitary adenoma, potentially leading to cardiovascular, renal, and bone complications. The management of this condition involves excision of the gland, with minimally invasive surgery being the standard of care. This requires accurate, high-quality preoperative imaging techniques. Among the most common techniques for adenoma localization are scintigraphy, ultrasound, computed tomography (CT), and magnetic resonance imaging (MRI). There is no consensus on the optimal diagnostic imaging algorithm, but the use of a CT protocol called 4D CT is a highly accurate and widely available alternative in centers in our country. A literature review was conducted on 4D CT of the parathyroid glands, with emphasis on protocol characteristics and the appropriate diagnostic analysis for the preoperative localization of adenomas in patients with hyperparathyroidism, including illustrative cases from our experience.

**Keywords:** Computed tomography. Contrast medium. Diagnostic imaging. Primary hyperparathyroidism. Parathyroid neoplasms. Parathyroidectomy.

#### Resumen

El hiperparatiroidismo primario se diagnostica por alteraciones de laboratorio y hasta en un 80% de los casos está causado por un adenoma solitario, pudiendo conducir a complicaciones cardiovasculares, renales y óseas. El manejo de esta condición es la escisión de la glándula, siendo la cirugía mínimamente invasiva el estándar de cuidado. Para ello es necesario contar con técnicas de imágenes preoperatorias precisas y de alta calidad. Dentro de las técnicas más frecuentes para la localización del adenoma se encuentran la cintigrafía, el ultrasonido, la tomografía computarizada (TC) y la resonancia magnética. No existe consenso acerca del algoritmo de imágenes diagnósticas óptimo, pero el uso de un protocolo de TC llamado TC 4D es una alternativa de alta precisión y ampliamente disponible en los centros de nuestro país. Se realiza una revisión de la literatura acerca de la TC 4D de paratiroides con énfasis en las características del protocolo y el análisis diagnóstico apropiado para la localización preoperatoria de adenomas en pacientes con hiperparatiroidismo, con casos ilustrativos de nuestra experiencia.

**Palabras clave:** Tomografía computarizada. Medio de contraste. Diagnóstico por imagen. Hiperparatiroidismo primario. Neoplasias paratiroides. Paratiroidectomía.

#### \*Correspondence:

Joaquín Cristi  
E-mail: jcrisip@udd.cl

Date of reception: 31-01-2025  
Date of acceptance: 19-06-2025  
DOI: 10.24875/AJI.25000007

Available online: 28-04-2026  
Austral J. Imaging. (Engl. ed.). 2026;32(2):73-79  
[www.resochradi.com](http://www.resochradi.com)

2810-708X / © 2025 Sociedad Chilena de Radiología. Published by Permanyer. This is an open access article under the CC BY-NC-ND license (<https://creativecommons.org/licenses/by-nc-nd/4.0/>).

## Introduction

Hyperparathyroidism is defined as an elevation of the circulating parathyroid hormone, which causes increased osteoclastic activity, leading to greater bone resorption. It can present as a primary, secondary, or tertiary disease. Primary hyperparathyroidism is caused by a solitary adenoma in up to 80% of cases; the remainder is divided among multiglandular hyperplasia, multiple adenomas, and parathyroid carcinoma<sup>1</sup>. Its incidence is 2 to 3 times higher in women than in men, and it increases with age, occurring mostly in those over 50 years of age<sup>2</sup>.

The diagnosis of primary hyperparathyroidism is made based on laboratory abnormalities. Symptoms are generally vague, and it is sometimes difficult to distinguish between symptomatic and asymptomatic patients<sup>3</sup>.

It can lead to cardiovascular complications (hypertension, arrhythmias, ventricular hypertrophy, vascular and valvular calcification), renal complications (nephrolithiasis and kidney damage), and bone complications (osteoporosis and vertebral fractures).

The management of this condition is excision of the gland. The correction of laboratory parameters and symptoms has been demonstrated after surgical treatment. Up to one-third of asymptomatic patients under active surveillance present disease progression; therefore, surgery is indicated in symptomatic and asymptomatic patients who meet certain specific criteria<sup>2,4</sup>.

Previously, surgical exploration of all four glands and excision were performed, with a reported accuracy of up to 95%. However, given its complications, minimally invasive parathyroidectomy is now the standard approach. To achieve this, the surgeon requires a precise localization of the suspicious gland, so it is necessary to have specific, high-quality preoperative imaging techniques<sup>5</sup>.

## Preoperative localization techniques

Traditional techniques for detecting a solitary adenoma include ultrasound (US) and scintigraphy with Tc99m sestamibi, either in uniplanar mode, single-photon emission computed tomography (SPECT) or SPECT/CT. The most widely accepted scintigraphy protocol consists of a biphasic acquisition, which allows for the recognition of early uptake and late washout of the radiotracer by the adenoma, enabling its differentiation from the thyroid tissue. In the last

decade, the detection of adenomas using a computed tomography (CT) protocol called 4D<sup>6</sup> has become popular. This protocol was first published in 2006 and consists of a multiphase and multiplanar neck CT scan, with a reconstruction on three planes associated with a dynamic evaluation after contrast administration, which corresponds to the fourth dimension<sup>7</sup>. Several studies have evaluated the accuracy of these techniques, demonstrating a sufficient and comparable performance<sup>8</sup>.

There is no consensus on the most appropriate diagnostic imaging algorithm for locating a parathyroid adenoma in the context of a primary hyperparathyroidism. In fact, international guidelines for the management of these patients recognize this situation and a high degree of regional variability, therefore they suggest that each practitioner decide on the localization modality based on their local knowledge and experience<sup>2,4</sup>. Traditionally, a combination of ultrasound (US) and scintigraphy has been used as the first-line diagnostic tool, reserving 4D CT for cases where these are inconclusive and in patients with persistent primary hyperparathyroidism following a parathyroidectomy<sup>9</sup>.

US is the initial technique of choice due to its low cost, wide availability, and lack of radiation exposure. Precisely, radiation exposure has been one of the main disadvantages of 4D CT mentioned in several studies, which is why it remains a second-line tool. However, when analyzing the techniques together, a cost-effectiveness and economic analysis study has suggested a more favorable cost-effectiveness when using US and 4D CT simultaneously as a study strategy, compared to 4D CT alone and US alone or in combination with scintigraphy<sup>10</sup>. This is because a false negative or the presence of multiglandular disease would lead to a greater number of extended cervical scans, with a consequently higher associated cost.

Because 4D CT has long been considered a second-line imaging modality, studies measuring its accuracy as a first-line technique and comparisons with ultrasound and scintigraphy are scarce and inconclusive. However, two meta-analyses, the most recent conducted in 2022, conclude that the available evidence suggests greater sensitivity, specificity, and positive and negative predictive values for 4D CT compared to ultrasound and scintigraphy as first-line methods alone<sup>11,12</sup>.

As a group, we propose considering 4D CT in conjunction with ultrasound as a first-line localization algorithm in centers that lack scintigraphy equipment or have limited access to it.

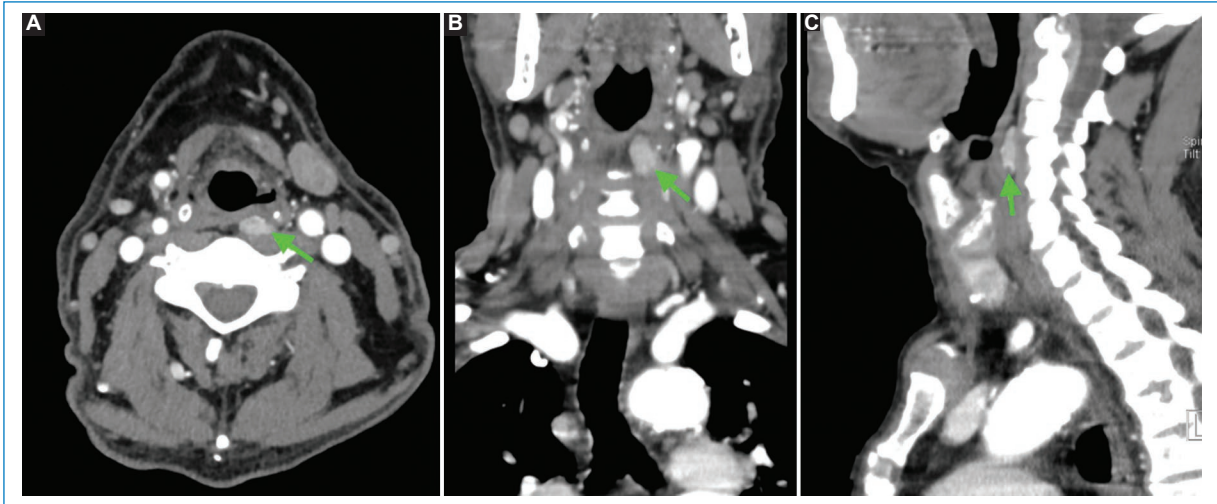


**Figure 1.** Axial (A), coronal (B), and sagittal (C) images from a 4D computed tomography scan of the parathyroid gland in the arterial phase, showing a left parasagittal nodular lesion in the retropharyngeal space at the level of the pyriform sinus, consistent with an ectopic parathyroid adenoma (arrows).

### Description of the 4D CT technique

4D CT is named for the detailed reconstruction using isovolumetric voxels, which allows for a precise localization of the suspicious lesion on the axial, coronal, and sagittal planes, as well as a dynamic study with intravenous contrast (Fig. 1). Several 4D CT protocols have been published, and most agree on performing a non-contrast phase followed by an arterial and portovenous phase. The examination, at least in one acquisition, should encompass the entire neck from the base of the skull to the mediastinum, due to the possible presence of ectopic adenomas, which can be found anywhere from the carotid bifurcation to the aortopulmonary window<sup>13</sup>. Some protocols plan the non-contrast phase from the hyoid bone to the sternoclavicular joint, combining it with wider contrast-enhanced phases from the angle of the mandible to the carina, to reduce the radiation dose. Injections of 75 ml of iso-osmolar contrast at a rate of 4 ml/s followed by a 25 ml bolus of saline solution are described<sup>6</sup>. The arterial phase is acquired 25-30 seconds after the injection, and the venous phase at 80 seconds. Some studies report the usefulness of a delayed phase at 300 seconds to better demonstrate washout<sup>6,14</sup>. If a bolus tracking system is available, the arterial phase is triggered 15-20 seconds after the contrast agent reaches the aorta, and the venous phase 40 seconds after the arterial phase<sup>15</sup>. A fine

slice thickness (0.625 mm), a rotation time of 0.4 seconds, a Pitch of 0.516:1, a field of view (FOV) of 20-35 cm, and 120-140 kV with an automatic current modulator are typically used<sup>6,14</sup>. Subsequently, the images are reconstructed at a greater thickness (2.5 mm) on all three axes. In our experience, an average dose-length product observed in these studies is between 5 and 15 mGy/cm.

### Analysis and diagnostic approach

The parathyroid glands are divided into superior and inferior glands, originating from the fourth and third branchial arches, respectively, which are located at the level of the carotid bifurcation. During fetal development, the parathyroid glands descend and the superior glands follow the thyroid, while the inferior glands follow the thymus. This explains why ectopic adenomas can be found along this entire path.

Classically, a parathyroid adenoma presents as an oval or rounded nodule with soft tissue density, hypodense to the thyroid tissue on non-contrast imaging (due to the higher iodine concentration in the latter), with intense enhancement on arterial imaging and washout on venous imaging (Fig. 2).

To identify it, we must use the arterial phase, looking in the most frequent location adjacent to the posterior border of the thyroid gland. Up to 25% of cases are ectopic, so we must remember the embryonic development described earlier. Upon recognizing it, the detailed

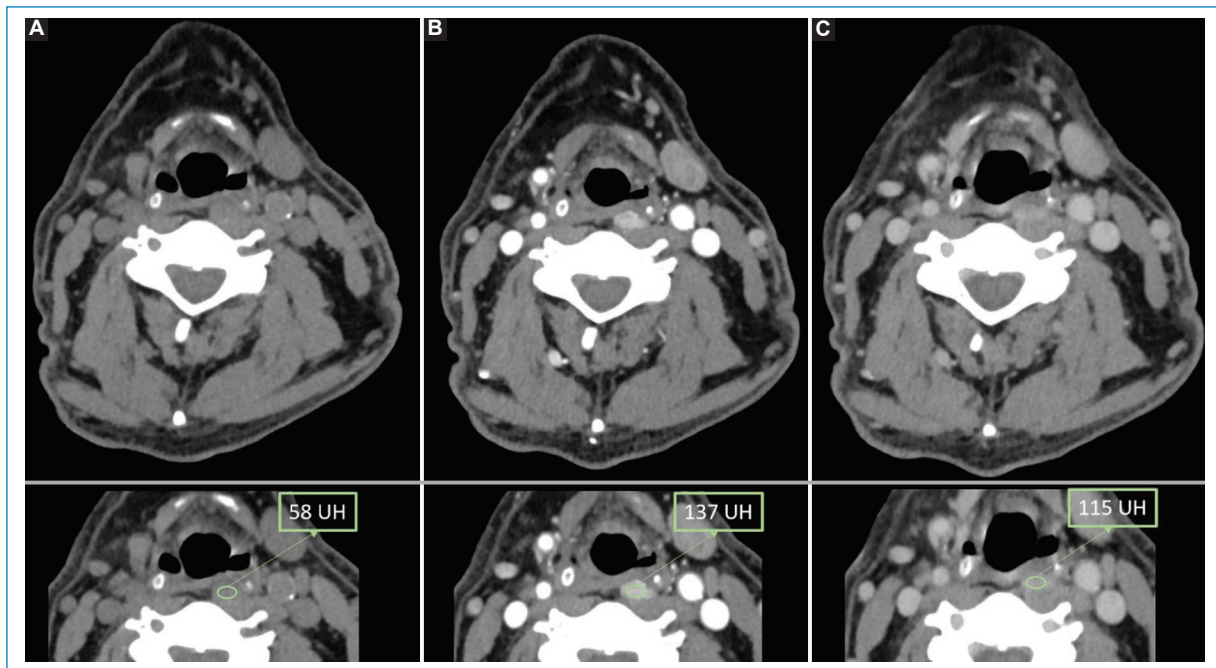


**Figure 2.** Dynamic 4D computed tomography scan of the parathyroid glands in non-contrast (A), arterial (B), and venous (C) phases, showing the characteristic enhancement pattern of a parathyroid adenoma, with intense enhancement on the arterial phase and washout on the venous phase.

location on the three planes should be described to allow the surgical team a precise approach, as well as its relationship to key structures to prevent complications, such as the thyroid (specify whether or not there is contact), the inferior thyroid artery, the carotid sheath, the trachea, and the tracheoesophageal groove. When one adenoma is found, it is important to continue searching for others, since up to 10% of cases are multiple.

A correct dynamic evaluation after contrast administration will allow the adenoma to be distinguished from other structures, such as normal thyroid tissue, thyroid nodules, and lymph nodes. Classically, unlike adenomas, lymphoid tissue shows a progressive enhancement with maximum attenuation in the late venous phase. However, it is also possible to observe an arterial phase enhancement that persists into the venous phase (Fig. 3). Normal thyroid tissue, although it shows avid enhancement in the arterial phase, similar to adenomas, maintains or increases its attenuation in the venous phase and also shows high density in the non-contrast phase (Fig. 4).

A study analyzing 33 adenomas using this technique provided attenuation values for each phase, comparing

them to normal thyroid tissue, highlighting significantly different values in the non-contrast phase. Arterial and venous washout values were also calculated from a late arterial phase (25 s), early venous (80 s), and late venous (5 min) phase, and significant differences in arterial washout (arterial vs. late venous phase) were highlighted, with suggested absolute and relative washout cutoff values of  $\geq 69\%$  and  $\geq 43\%$ , respectively, for the adenomas<sup>14</sup>.

In intrathyroidal adenomas, ultrasound plays an important complementary role, as it allows for a more complete characterization of the suspicious lesion, it can identify concurrent thyroid nodules, and as a support to perform preoperative biopsies that confirm the diagnosis (Fig. 5).

In our country, there is limited literature on this topic, consisting mainly of case reports and some reviews on hyperparathyroidism and the management of adenomas<sup>16-18</sup>. There are also few publications specifically dedicated to the available techniques. A review presents two cases of adenomas identified using SPECT/CT, but this method is significantly less available than CT in our country and the rest of Latin America, and as we have mentioned, it has not demonstrated better accuracy or

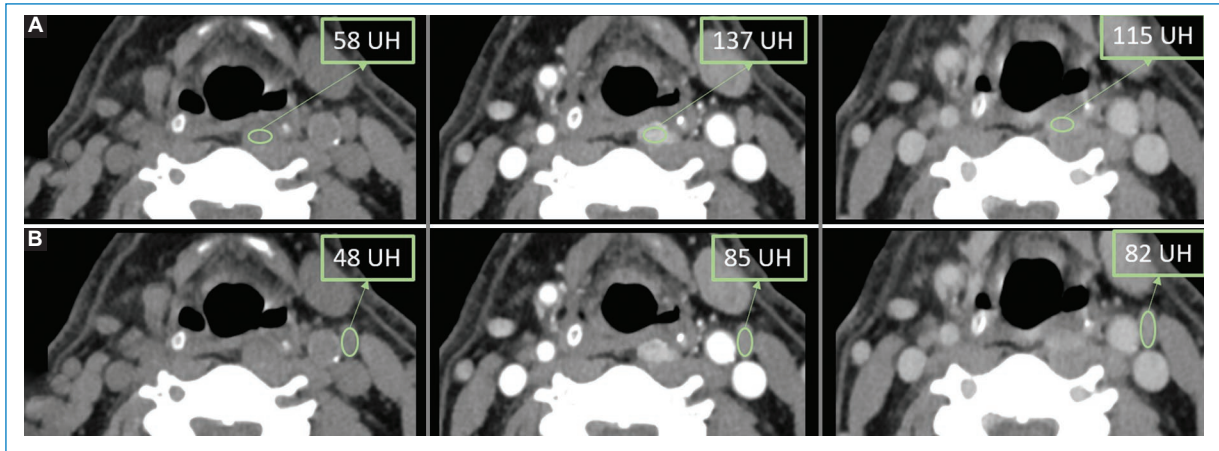


**Figure 3.** Comparison of the behavior in dynamic ultrasound of a parathyroid adenoma (A) and a lymph node (B) in non-contrast arterial and venous phases, from left to right, respectively. An adenoma shows intense enhancement in the arterial phase and washout in the venous phase, unlike the lymph node, which exhibits less enhancement in the arterial phase with no significant change in the venous phase.

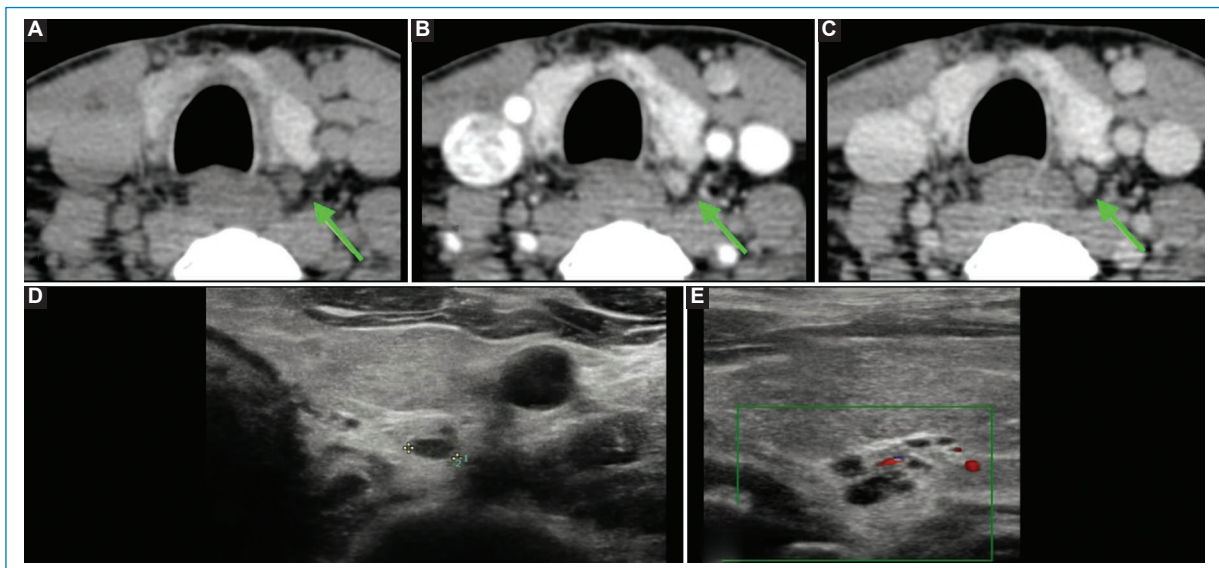


**Figure 4.** Complement to the 4D computed tomography (CT) and ultrasound (US) in the detection of parathyroid adenomas. CT in non-contrast (A), arterial (B), and venous (C) phases showing a left retrothyroid lesion suspicious for an adenoma (arrows), with its classic behavior in the dynamic study, highlighting its lesser spontaneous attenuation compared to the thyroid tissue. Correlation of the lesion on US on the transverse (D) and longitudinal (E) planes, with similar morphology, homogeneous and hypoechoic.

cost-effectiveness compared to 4D CT<sup>18</sup>. In figure 6 we show a challenging case in which SPECT/CT was negative and the use of 4D CT combined with ultrasound was key to locating a parathyroid adenoma. After

histological confirmation by fine-needle aspiration biopsy and surgical excision, a lesion compatible with an atypical parathyroid adenoma, measuring 7 mm in its largest diameter, was displayed.

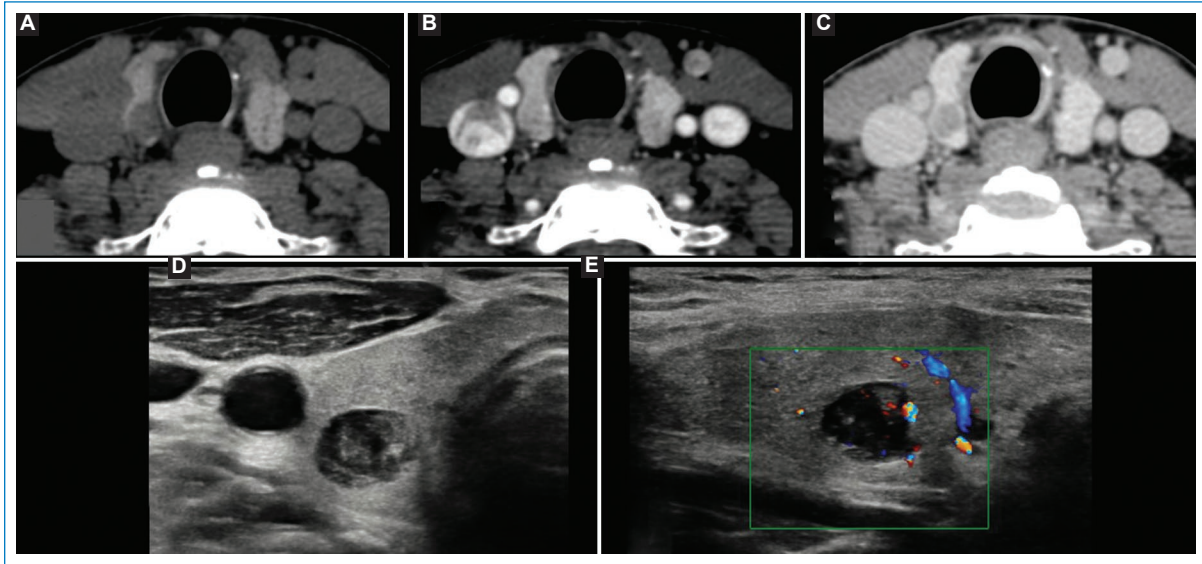


**Figure 5.** Ultrasound (US) as a guide for biopsy of lesions suspected of being adenomas. Computed tomography in non-contrast (A), arterial (B), and venous (C) phases showing a right intrathyroidal lesion with typical adenoma behavior in the dynamic study. Ultrasound correlation on the transverse (D) and longitudinal (E) planes allowed for a biopsy with a compatible result.

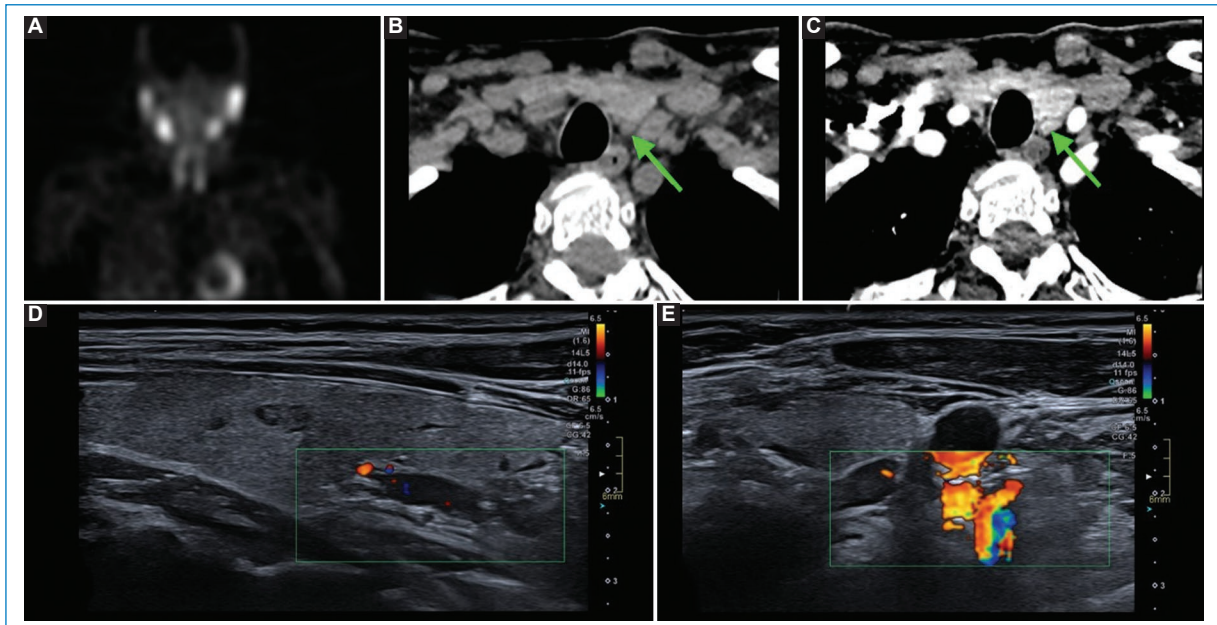


**Figure 6.** Complementary techniques for the diagnosis of parathyroid adenomas. MIP image (A) from a single-photon emission computed tomography (SPECT) MIBI scan in which no hyperenhancing lesions suggestive of an adenoma were shown. 4D computed tomography in non-contrast (B) and arterial (C) phases showing a small left retrothyroid nodule with early enhancement in the arterial phase (arrows). Ultrasound images on the longitudinal (D) and transverse (E) axes, showing a hypoechoic, elongated, left retrothyroid nodular lesion with poor vascularization, which corresponded to an adenoma in both the biopsy and the final surgical specimen.

## Conclusion

There is still no consensus on the most appropriate algorithm for the preoperative identification of parathyroid adenomas. The reported high accuracy of 4D CT positions it as a first-line alternative, sometimes demonstrating greater cost-effectiveness compared to other localization strategies. The technique is based on performing multiplanar reformatting along with dynamic analysis of glandular behavior with contrast, which differentiates adenomas from the thyroid gland and adjacent lymph nodes, the main differential diagnoses. Knowledge of and familiarity with this technique are essential to increase the possibility of localizing parathyroid adenomas in centers in our country.

## Funding

The authors declare that they have not received funding.

## Conflicts of interest

The authors declare no conflicts of interest.

## Ethical considerations

**Protection of human subjects and animals.** The authors declare that no experiments on humans or animals were performed for this research.

**Confidentiality, informed consent, and ethical approval.** The authors have followed their institution's confidentiality protocols, obtained informed consent from all patients, and secured approval from the Ethics Committee. SAGER guidelines have been followed as applicable to the nature of the study.

**Declaration on the use of artificial intelligence.** The authors declare that no generative artificial

intelligence was used in the writing or creation of the content of this manuscript.

## References

- Jategaonkar AA, Lerner DK, Cooke P, Kirke D, Genden EM, Trosman SJ. Implementation of a 4-dimensional computed tomography protocol for parathyroid adenoma localization. *Am J Otolaryngol.* 2021;42:102907.
- Wilhelm SM, Wang TS, Ruan DT, Lee JA, Asa SL, Duh QY, et al. The American Association of Endocrine Surgeons guidelines for definitive management of primary hyperparathyroidism. *JAMA Surg.* 2016;151:959-68.
- Bilezikian J, Silverberg S. Asymptomatic primary hyperparathyroidism. *N Engl J Med.* 2004;350:1746-51.
- Rubin MR, Bilezikian JP, McMahon DJ, Jacobs T, Shane E, Siris E, et al. The natural history of primary hyperparathyroidism with or without parathyroid surgery after 15 years. *J Clin Endocrinol Metab.* 2008; 93:3462-70.
- Bilezikian JP, Khan AA, Silverberg SJ, Fuleihan GEH, Marcocci C, Minisola S, et al. Evaluation and management of primary hyperparathyroidism: summary statement and guidelines from the Fifth International Workshop. *J Bone Miner Res.* 2022;37:2293-314.
- Zander D, Bunch PM, Policeni B, Juliano AF, Carneiro-Pla D, Dubey P, et al. ACR Appropriateness Criteria® Parathyroid Adenoma. *J Am Coll Radiol.* 2021;18:S406-22.
- Hoang JK, Sung WK, Bahl M, Phillips CD. How to perform parathyroid 4D CT: tips and traps for technique and interpretation. *Radiology.* 2014;270:15-24.
- Rodgers SE, Hunter GJ, Hamberg LM, Schellingerhout D, Doherty DB, Ayers GD, et al. Improved preoperative planning for directed parathyroidectomy with 4-dimensional computed tomography. *Surgery.* 2006;140:932-41.
- Solorzano CC, Carneiro-Pla D. Minimizing cost and maximizing success in the preoperative localization strategy for primary hyperparathyroidism. *Surg Clin North Am.* 2014;94:587-605.
- Xu F, Pastakia B, Liu F. Incremental value of CT in the localization of parathyroid adenomas. *Radiol Case Rep.* 2015;10:925.
- Lubitz CC, Stephen AE, Hodin RA, Pandharipande P. Preoperative localization strategies for primary hyperparathyroidism: an economic analysis. *Ann Surg Oncol.* 2012;19:4202-9.
- Cheung K, Wang TS, Farrokhyar F, Roman SA, Sosa JA. A meta-analysis of preoperative localization techniques for patients with primary hyperparathyroidism. *Ann Surg Oncol.* 2012;19:577-83.
- Kattar N, Mignerone M, Debaquey MS, Haidari M, Pou AM, McCoull ED. Advanced computed tomographic localization techniques for primary hyperparathyroidism: a systematic review and meta-analysis. *JAMA Otolaryngol Head Neck Surg.* 2022;148:448-56.
- Parikh AM, Suliburk JW, Morón FE. Imaging localization and surgical approach in the management of ectopic parathyroid adenomas. *Endocr Pract.* 2018;24:589-98.
- Wazzan M. Absolute and relative washout rates associated with parathyroid adenoma. *Cureus.* 2023;15:e48947.
- Vijayasarithi A, Karnezis S, Azizyan A, Salamon N, Sepahdari A. 4D CT parathyroid for the general radiologist: a pictorial essay of illustrative cases. *Curr Probl Diagn Radiol.* 2022;51:659-65.
- Luis RA, Claudio BB. Mediastinal ectopic parathyroid adenoma, a case report. *Rev Cir Mex.* 2023;75:225-6.
- Rappoport DW, Caballero QMG, Cortés BN, Cabané TP, Gac EP, Rodríguez MF. Primary hyperparathyroidism. *Rev Cir Mex.* 2021;73:222-6.

## Diffusion-weighted imaging for the head-neck region and spinal cord: echo planar and non-echo planar imaging technique

### Imagen ponderada en difusión para la región de cabeza-cuello y médula espinal: técnica de imagen eco planar y no eco planar

Gonzalo Araya-Rojas<sup>1</sup>, Rodrigo Araya-Rojas<sup>2,3</sup>, and Pablo Maturana-Quijada<sup>4\*</sup> 

<sup>1</sup>Imaging Department, Clínica Alemana de Santiago, Santiago; <sup>2</sup>Faculty of Medicine, Universidad Católica del Norte, Antofagasta; <sup>3</sup>Imaging Service, Hospital San Pablo de Coquimbo, Coquimbo; <sup>4</sup>School of Medical Technology, Faculty of Medicine and Healthcare Sciences, Universidad Mayor, Santiago, Chile

#### Abstract

In the last decade, diffusion imaging has gained ground in applications for head, neck, and spinal cord imaging; however, it remains a tool with limitations. The technique is susceptible to certain artifacts, such as geometric distortion, wrap-around (aliasing) artifacts, magnetic susceptibility effects, incomplete fat saturation, and motion artifacts due to patient movement, in addition to exhibiting a lower spatial resolution and signal-to-noise ratio compared to conventional T1- and T2-weighted sequences. This sometimes makes precise anatomical localization of the pathology challenging. These limitations have led many radiologists to consider that its routine implementation in the head and neck region still needs further development to obtain a good image. In recent years, the acquisition methods for the technique have been perfected, which has allowed for improvements in the artifacts present in the early images. The aim of this paper is to present a review of the new commercially available techniques that are based on non-echo planar acquisitions, defining their image acquisition methods, applications, advantages, and disadvantages.

**Keywords:** Magnetic resonance imaging. Diffusion-weighted imaging. Echo-planar imaging. Apparent diffusion coefficient.

#### Resumen

En la última década, la imagen de difusión ha ganado terreno en aplicaciones de imágenes de cabeza, cuello y médula espinal; sin embargo, sigue siendo una herramienta con limitaciones. La técnica es susceptible a ciertos artefactos, como distorsión geométrica, artefactos de envolvimiento, efectos de susceptibilidad magnética, saturación incompleta de la grasa y artefactos por el movimiento del paciente, además de presentar una resolución espacial y una relación señal-ruido más baja en comparación con las secuencias convencionales ponderadas en T1 y T2. Esto hace que, en ocasiones, la localización anatómica precisa de la patología sea un desafío. Estas limitaciones han llevado a que muchos radiólogos consideren que a la implementación sistemática en la cabeza y el cuello todavía le falta desarrollo para obtener una buena imagen. Durante los últimos años se han perfeccionado los métodos de adquisición de la técnica, lo que ha permitido mejorar los artefactos propios de las primeras imágenes. El objetivo de este trabajo es presentar una revisión de las nuevas técnicas disponibles comercialmente que se basan en adquisiciones no eco planares, definiendo su forma de obtención de imagen, aplicaciones, ventajas y desventajas.

**Palabras clave:** Resonancia magnética. Imagen ponderada en difusión. Imagen eco planar. Coeficiente de difusión aparente.

#### \*Correspondence:

Pablo Maturana-Quijada  
E-mail: pablo.maturana@umayor.cl  
2810-708X / © 2025 Sociedad Chilena de Radiología. Published by Permanyer. This is an open access article under the CC BY-NC-ND license (<https://creativecommons.org/licenses/by-nc-nd/4.0/>).

Date of reception: 31-05-2025

Date of acceptance: 12-11-2025

DOI: 10.24875/AJI.25000041

Available online: 28-04-2026

Austral J. Imaging. (Engl. ed.). 2026;32(2):80-88

[www.resochradi.com](http://www.resochradi.com)

## Introduction

Diffusion-weighted magnetic resonance imaging (DWI) allows for the analysis of water molecule movement in biological tissues. In an homogeneous medium, water diffusion is random and isotropic, meaning it is equal in all directions. In contrast, in an environment like the human body, water is divided between cells and extracellular compartments. Water molecules in extracellular environments experience a relatively free diffusion, while the intracellular molecules exhibit a restricted diffusion, which is affected by pathological processes. Therefore, DWI provides qualitative and quantitative information on the microscopic movements of the water molecules and their diffusion properties, adding functional information to the anatomical sequences obtained with magnetic resonance imaging<sup>1</sup>.

DWI has become a standard method in the evaluation and diagnosis of acute stroke, and it also provides information about the cellularity, microstructures, and microvasculature, which is of great importance for cancer studies. This has led to the development of a variety of DWI acquisition techniques, which are generally classified as echo-planar imaging (EPI) and non-EPI techniques.

EPI is a type of rapid acquisition that has been widely used in DWI. It is characterized by the continuous application of gradients after an excitation pulse, allowing complete filling of the  $k$ -space during a single echo/excitation. The main advantage of single-shot EPI is the speed of image acquisition, which occurs in milliseconds. This speed is particularly critical in diffusion imaging, as it minimizes artifacts associated with patient movement, such as voluntary movements, respiration, and vascular pulsation, which can interfere with the acquired diffusion signal, which is highly sensitive to these types of movements<sup>2</sup>. However, since EPI relies on precise gradients to manipulate a single echo, it presents a significant drawback: it is highly sensitive to magnetic field inhomogeneities, which generate some image artifacts such as blurring (we will use this term to refer to low spatial resolution in the image) and geometric distortion. Both artifacts limit lesion detection in regions with large tissue interfaces (tissue/air) or in the presence of metallic medical implants, where some portions of the image can become difficult to interpret<sup>3</sup>. Due to this limitation of the EPI technique, non-EPI sequences use different acquisition strategies that improve DWI acquisition in regions with large tissue interfaces, thus avoiding image artifacts.

The aim of this review is to present a guide based on EPI and non-EPI techniques to evaluate regions that were previously difficult to study by DWI, such as the head-neck area and spinal cord.

## Conventional diffusion-weighted imaging

Currently, advances in DWI have evolved considerably since its initial applications in the study of cerebral ischemia. Significant efforts have been dedicated to the use of DWI in cancer. The applications of DWI in cancer are not limited to detection and diagnosis, but extend to staging, classification, treatment evaluation, and even prediction; this is because it allows for the generation of tissue contrast based on the microscopic and random movement of water molecules in the body. Under specific pathological conditions, the mobility of the water molecules is reduced<sup>4</sup>.

In some types of tumors, this restriction in diffusion is associated with high cell density or a higher nucleus-to-cytoplasm ratio, making reduced diffusivity an indirect indicator of increased tumor cellularity.

Based on these principles, diffusion-weighted imaging provides radiologists with useful tools for detecting inflammation and infections, improving the identification of neoplasms, characterizing tumor biology, and evaluating the response to treatments.

To generate diffusion-weighted images, the factor that controls the degree of diffusion weighting is called the  $b$  value (expressed in  $s/mm^2$ ). This  $b$  value reflects the strength and momentum of the gradients used to generate diffusion-weighted images. Typical  $b$  values range from 0 to approximately 4000  $s/mm^2$ . The simplest way to understand this value in DWI is to view it similarly to how the echo time choice affects T2 weighting.

One characteristic of choosing this  $b$  value is that the diffusion MRI signal progressively decreases as the  $b$  value increases (i.e., higher  $b$  values mean more noise in the image). However, the rate of this decrease varies depending on the  $b$  values used. With relatively low  $b$  values (e.g.,  $< 200 s/mm^2$ ), the signal attenuates rapidly due to the contribution of accelerated water motion in the capillaries, resulting in significant signal loss in addition to the diffusion effect itself<sup>5</sup>. This phenomenon makes low  $b$  values particularly sensitive to tissue vascularization, primarily microperfusion and microcirculation, and has only a limited influence on diffusion. As the  $b$  value increases, the contribution of capillary vasculature becomes negligible, leaving diffusion as the main attenuation mechanism.

In an intermediate  $b$  value range (between 500 and 1500  $\text{s/mm}^2$ ), signal attenuation mainly reflects the spatial scale of the cell size, making it a key indicator of cellularity, as shown in figure 1. When the  $b$  value is increased further, a greater sensitivity is achieved in smaller cell-scale structures. This makes diffusion magnetic resonance imaging a useful tool for assessing the microstructural complexity and heterogeneity of the tissue.

To date, there is no clear consensus in the literature regarding a defined threshold for high  $b$  values; however, it is considered that a  $b$  value  $> 2000 \text{ s/mm}^2$  is high in neurological studies, while values  $> 1000 \text{ s/mm}^2$  are used in body imaging applications<sup>4</sup>.

The optimal  $b$  value selection must balance the sensitivity to the diffusion phenomena, artifacts, and acquisition time. In head and neck applications, intermediate values ( $800\text{-}1200 \text{ s/mm}^2$ )<sup>5</sup> are typically used, which offer an adequate tissue differentiation without excessively compromising the *Signal-to-Noise Ratio* (SNR). In the spinal cord, where magnetic susceptibility and physiological movement are more critical, a more conservative range ( $500\text{-}800 \text{ s/mm}^2$ )<sup>6</sup> is recommended, avoiding distortion artifacts and maintaining reasonable acquisition times.

With low  $b$  values ( $< 200 \text{ s/mm}^2$ ), the signal contrast is dominated by the intravoxel incoherent motion, primarily reflecting capillary microperfusion. This range can be useful in multiparametric studies to estimate the perfusion fraction ( $f$ ) and pseudodiffusivity ( $D^*$ ), although it requires additional modeling. On the other hand, the high  $b$  values ( $> 1500 \text{ s/mm}^2$ ) accentuate the sensitivity to pure diffusive restriction and densely packed microstructures, but with a marked reduction in signal and an increase in noise.

In non-EPI techniques, which present less geometric distortion and better phase stability, it is possible to use higher  $b$  values with less penalty in image quality. However, it should be considered that increasing the number of  $b$  values or their magnitude can extend acquisition times and require greater patient cooperation or the use of motion correction strategies.

## ADC Map

The base of the DWI sequence maintains an intrinsic T2 weighting, meaning that the signal is influenced by both the diffusion effects and the T2 of the tissue. To reduce this ambiguity, a map is generated that integrates the information obtained from the diffusion sequence with a version of the same sequence without

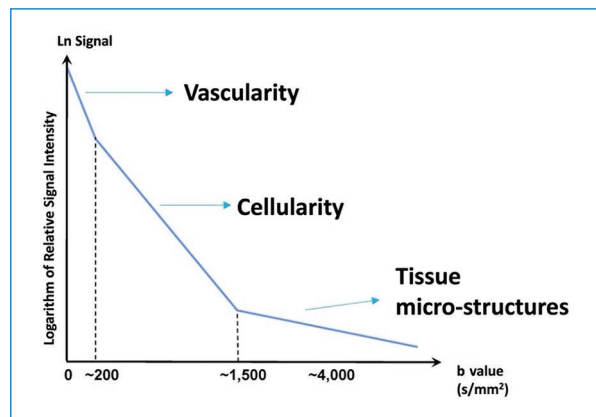


**Figure 1.** Signal attenuation due to diffusion as a function of the  $b$  value, divided into three regions: low, intermediate, and high  $b$  values. Each range is associated with a specific tissue property analyzable using DWI. The  $b$  values on the horizontal axis are for reference only and may vary depending on the application (adapted from Tang et al.<sup>4</sup>).

the diffusion gradients activated (image with  $b = 0$ ), called the Apparent Diffusion Coefficient (ADC) image, which is measured in  $\text{mm}^2 \text{ s}^{-1}$ . In this way, the T2-related effects are mathematically eliminated, allowing the acquisition of a purely parametric diffusion image.

The use of DWI images combined with ADC mapping allows differentiation between benign and malignant lesions. In general, malignant tumors tend to have lower mean ADC values than benign neoplasms, due to their high cell density, higher nucleus-to-cytoplasm ratio and more compact intercellular spaces. However, this is not an absolute rule, and there are frequent exceptions. Some benign lesions may show reduced diffusivity (abscesses, schwannomas, paragangliomas, meningiomas, solitary fibrous tumors, cholesteatomas, hemangiopericytomas, and myoepithelial tumors)<sup>7</sup>.

Several limitations are associated with reported mean threshold values for ADC due to the heterogeneity of the populations analyzed in the studies. Factors such as scanning parameters (e.g., higher  $b$  values), acquisition array size, and magnetic field strength, along with differences between equipment and manufacturers, affect the reproducibility of quantitative ADC measurements.

Despite these limitations, numerous studies have demonstrated that DWI represents a valuable and promising tool for assessing malignancy risk in head and neck lesions<sup>8,9</sup>. To address these limitations, some researchers have proposed using internal controls, such as bone marrow or spinal cord, to calculate a normalized ADC ratio<sup>5</sup>.

## EPI technique for DWI

Single-shot Echo Planar Imaging (SSH-EPI) is commonly used in DWI due to its high acquisition speed (50-100 ms) and low sensitivity to phase errors induced by patient movement, allowing for a large number of diffusion directions or multiple  $b$  values within a short scan time. The technique is based on filling all  $k$ -space lines in a single shot, meaning that the acquisition is completed within one repetition time. However, it has limitations, such as low image quality, blurring effect, low signal-to-noise ratio (SNR), artifacts such as chemical shift, magnetic susceptibility, and geometric distortion at tissue/air interfaces due to  $B_0$  inhomogeneities. These problems intensify with high magnetic fields<sup>3</sup>.

The two typical image artifacts consistently observed in SSH-EPI are blurring and image distortion. The spatial resolution of SSH-EPI is severely affected by the  $T2^*$  dephasing of the tissue, which generates signal loss at the outer edges of the  $k$ -space (the region corresponding to high frequencies, i.e., image detail); this weighting introduces image blurring. Therefore, it is recommended to always use the lowest echo spacing value to avoid this blurring.

The other artifact present in SSH-EPI is image distortion, which occurs mainly in regions with strong inhomogeneity of the local magnetic field (e.g., skull base, tissue/air boundaries). This generates a misplaced signal in the phase-encoding direction due to the lack of homogeneity of the main field, and the net field deviates from the desired linear shift, leading to incorrect voxel mapping<sup>10</sup>.

Parallel imaging techniques, such as SENSE (Sensitivity Encoding), have been shown to improve the quality of SSH-EPI by reducing geometric distortion artifacts. However, SENSE can present lower signal-to-noise ratios (SNRs) and artifacts associated with high acceleration factors ( $R$ )<sup>11</sup>.

Recent studies indicate that the Compressed Sensing (CS) technique, which is based on the acquisition of a balanced random under-sampling with iterative noise removal, resolves these problems and improves image quality with high  $R$  factors compared to the conventional SENSE<sup>12</sup> technique. Furthermore, EPI with compressed SENSE has been shown to improve the contrast-to-noise ratio, ADC values, image distortion, and artifacts in diffusion-weighted MRI images of the head and neck<sup>13</sup>.

## Multi-shot EPI (MS-EPI) technique

To reduce artifacts produced by SSH-EPI, variants such as multi-shot EPI have been introduced. In this modality,  $k$ -space filling is performed in segments via multiple repetitions (shots), which allows to reduce susceptibility artifacts and improve both spatial resolution and signal-to-noise ratio (SNR). Unlike SSH-EPI, if the  $k$ -space is filled with more than one repetition time, it is called a *multishot* EPI or segmented EPI technique, which takes samples of  $k$ -space over multiple EPI trajectories with widely spaced lines that interleave to cover the entire  $k$ -space.

However, this improvement comes at the cost of a longer acquisition time compared to SSH-EPI. Diffusion signals are inherently sensitive to patient movement because diffusion preparation gradients encode minute (molecular) movements in the phase of the signal; even small movements of the subject (e.g., heart rate, respiration) during diffusion preparation can lead to a spatially variable phase unrelated to the diffusion<sup>10</sup>.

For this reason, non-EPI sequences are presented as an option for the susceptibility artifacts present in the EPI sequences.

## Non-EPI techniques for DWI

The commercially available non-EPI DWI techniques, with their advantages and disadvantages compared to EPI techniques, are (Table 1):

- Readout-Segmented-Echo Planar Imaging (rs-EPI).
- HASTE DWI sequence (Half-Fourier Acquisition Single-shot Turbo spin Echo).
- PROPELLER DWI sequence (Periodically Rotated Overlapping Parallel Lines with Enhanced Reconstruction).
- Reduced Field of View (FOV) imaging (rFOV or zoom).

A description of the technical aspects of each of these sequences is presented below.

### *rs-EPI*

rs-EPI uses a series of EPI acquisitions to cover the  $k$ -space in a mosaic-like pattern<sup>14</sup>. Instead of acquiring all  $k$ -space lines in a single shot, as SSH-EPI does, rs-EPI divides the acquisition into several shots, each one with fewer  $k$ -space lines. This reduces echo spacing and echo train length, resulting in a reduction of

**Table 1.** Commercially available non-EPI DWI techniques, highlighting their advantages and disadvantages compared to the DWI EPI sequence

Technique	Acronym	Key characteristics	Advantages	Disadvantages	Trade name
Half-Fourier Acquisition Single-shot Turbo spin Echo	HASTE	Based on a single-shot turbo spin echo, with <i>half Fourier</i> technique	Improves image quality in head and neck pathologies due to the reduction of susceptibility artifacts <sup>24</sup>	Lower tumor visibility, lower SNR and noise contrast; longer acquisition time <sup>24</sup>	Siemens Healthineers: HASTE General Electric Healthcare: Single Shot-FSE Philips Healthcare: Single Shot-TSE Canon Medical Systems: FASE
DWI with segmented EPI readout	rs-EPI	Multi-shot echo-planar imaging technique	High diagnostic accuracy for cholesteatoma; effective in complex diagnostic scenarios <sup>25</sup>	Cannot completely replace non-EPI DWI; requires a combined use to improve sensitivity <sup>25</sup>	Siemens Healthineers: RESOLVE
Periodically Rotated Overlapping Parallel Lines with Enhanced Reconstruction	PROPELLER	Periodically rotated overlapping parallel lines with enhanced reconstruction	Free of geometric distortion; robust against motion artifacts <sup>26</sup>	Long scan times and high SAR, especially in high magnetic fields <sup>26</sup> ; star artifact appearance at low oversampling values	Siemens Healthineers: BLADE General Electric Healthcare: PROPELLER Philips Healthcare: Multivane Canon Medical Systems: JET
DWI with reduced field of view (FOV)	rFOV	Uses a limited field of view to improve spatial resolution.	Higher spatial image resolution, FOV optimized to small regions, reduced artifacts, and improved lesion visibility <sup>27</sup>	Lower SNR compared to full-field-of-view DWI, longer acquisition time <sup>27</sup>	Siemens: iZOOM General Electric Healthcare: ZOOMit Philips Healthcare: iZOOM

BLADE: Balanced Steady State Free Precession Line Acquisition with Undersampling; FASE: Fast Advanced Spin Echo; FSE: Fast Spin Echo; RESOLVE: Readout Segmentation of Long Variable Echo trains; SAR: Specific Absorption Rate; SNR: Signal-to-Noise Ratio; TSE: Turbo Spin Echo.

both the geometric distortion and T2\* *blurring*, and increases the SNR<sup>15</sup>.

The disadvantage is that, by using more than one shot, the scan time required to form the image is longer, which can generate more movement in the patients. A comparison of rs-EPI with SSH-EPI demonstrates an improvement in regions that have a strong difference in magnetic susceptibility, such as the temporal lobes and brainstem in the brain<sup>16</sup>. Figure 2 shows a comparison of acquisitions with EPI techniques.

### HASTE DWI

This technique uses an SSH-TSE (Single-Shot Turbo Spin Echo) method to acquire images. As a single-shot sequence, it shares with EPI a low sensitivity to movement, although with a slightly longer acquisition time. However, being spin-echo based, this technique avoids the image distortion and susceptibility artifacts characteristics of SSH-EPI-based techniques. Its unique echo train is significantly longer than that of the EPI, which

can lead to a loss of image quality due to T2\* decay during acquisition<sup>17</sup>. To mitigate this problem, HASTE DWI uses a half-Fourier strategy that shortens the echo train, decreasing the impact of T2 blurring, although with an adverse or moderate effect on the SNR.

The advantage of this technique over EPI is that it is unaffected by the susceptibility or chemical shift. However, HASTE DWI images have certain disadvantages, such as the blurring associated with T2 decay and low SNR, although these can be compensated for by optimizing image parameters such as the array size, effective echo time, echo space, and receiver bandwidth. A wide bandwidth and a small array size improve SNR; a wide bandwidth also improves the ADC's discrimination capability<sup>18</sup>.

### PROPELLER DWI

PROPELLER is based on a turbo spin echo (TSE) sequence<sup>19</sup>. Standard TSE sequences fill the *k*-space in a rectilinear or Cartesian pattern. Therefore, the

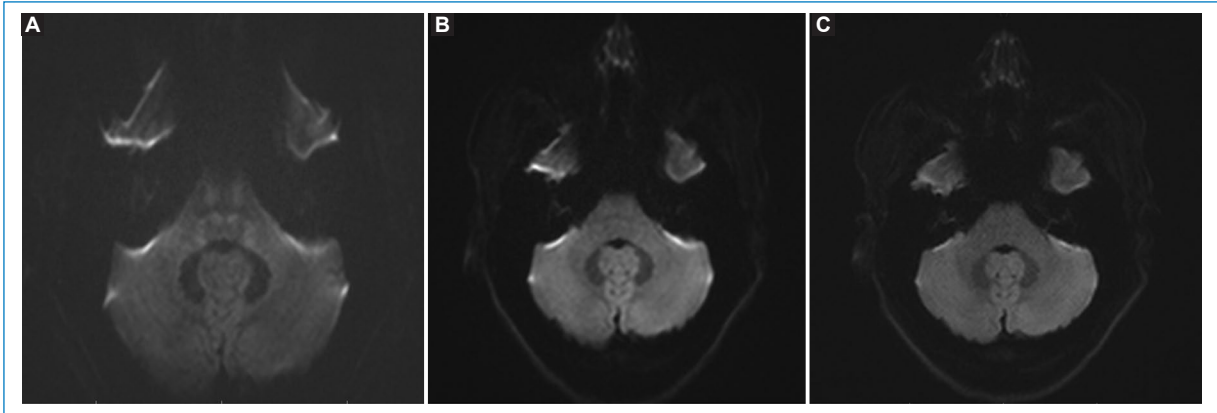


**Figure 2.** Evaluation of EPI and non-EPI techniques at the skull base. **A** and **B**: show diffusion-weighted imaging with the EPI technique; and **C**: with a non-EPI technique. **A**: SSH-EPI, with an acquisition time of 1:10 min. **B**: MS-EPI diffusion-weighted imaging, with an acquisition time of 1:57 min. **C**: Acquisition using the RESOLVE technique, with an acquisition time of 3:20 min. All images were acquired on a Siemens Skyra 3T scanner.

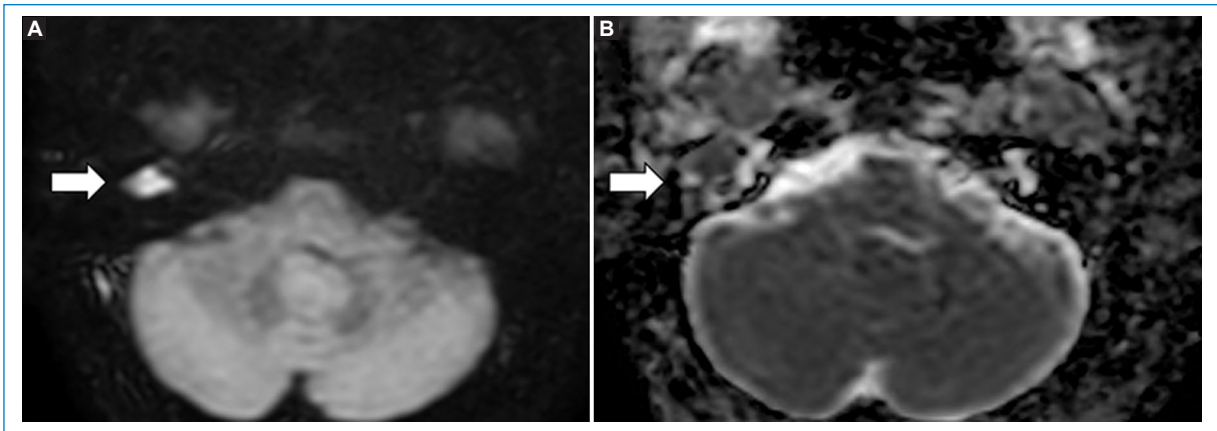


**Figure 3.** Phillips 1.5T TSE Axial MultiVane Diffusion. A lesion (**A**: DWI; **B**: ADC map) exhibiting restricted diffusion, consistent with a middle ear cholesteatoma in the epitympanum, is delimited (arrows).

$k$ -space center data are acquired once or according to the number of averages (NSA or NEX). Information from the  $k$ -space center has important characteristics about the image quality that are affected by movement of the patient.

The PROPELLER sequence uses radial (non-Cartesian) sampling of  $k$ -space, with parallel data lines (also called “blades”) that rotate around the  $k$ -space center, facilitating the correction of spatial inconsistencies. A key strength of PROPELLER is its self-navigation; that is, all the blades cover the center of the  $k$ -space, which is oversampled, allowing for the estimation of motion-induced phase errors for each acquisition and the discarding of that information.

PROPELLER significantly improves image quality and reduces motion artifacts. These sequences can be superior to rs-EPI methods, in which susceptibility artifacts are more problematic<sup>20</sup>. However, the use of TSE increases the specific absorption rate and produces more tissue heating compared to gradient-echo EPI methods.

### **rFOV**

rFOV techniques function similarly to parallel imaging by reducing the acquisition of phase-encoded lines. In rFOV, aliasing is avoided by excluding signals outside of a selected volume, using strategies such as inner volume imaging (IVI), outer volume suppression (OVS), and multidimensional radiofrequency (RF) excitation.

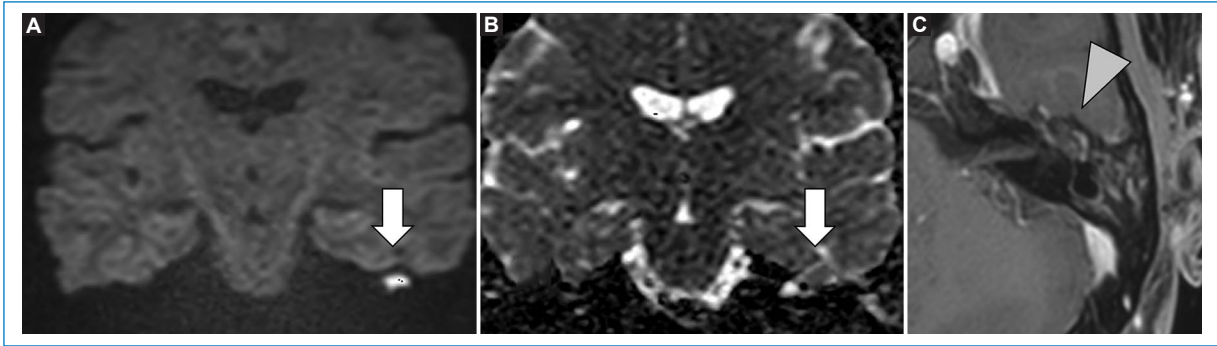


**Figure 4.** Phillips 1.5T TSE Axial MultiVane Diffusion. **A** and **B**: left epitympanic cholesteatoma with coronal diffusion restriction non-EPI (arrows). **C**: absence of enhancement on T1 acquisition after gadolinium (arrowhead).

IVI is based on the superposition of excited and refocused volumes, allowing the field of view to be limited and its application to be extended from single slices to multiple interleaved slices<sup>21</sup>. OVS, on the other hand, eliminates signals outside the region of interest using spatially selective RF pulses<sup>22</sup>. Finally, multidimensional excitation, with selective 2D RF pulses, expands slice coverage and improves visualization, especially in the spinal cord, compared to the standard SSH-EPI<sup>23</sup>. This technique requires additional fat saturation and can benefit from parallel transmissions to optimize the acquisition times.

### Clinical examples of non-EPI techniques

To illustrate the diagnostic advantages of non-EPI diffusion-weighted imaging sequences in complex clinical scenarios, several representative cases are presented below (Figs. 3 to 8). These images demonstrate how these techniques contribute to improving anatomical delineation and reducing artifacts inherent in conventional EPI-based acquisitions.

Figures 3 and 4 show studies of patients with cholesteatomas, in which the use of non-EPI sequences facilitates the differentiation between pathological tissue and adjacent structures due to reduced geometric distortion, optimizing lesion detection and characterization. Figures 5 and 6 correspond to a left paraspinal inflammatory process with increased volume of the retropharyngeal space, in which the reduction of geometric distortions allowed for better definition of the extent of the inflammatory involvement. Figure 7 exemplifies the application of these techniques in a mandibular keratocyst, demonstrating the ability of non-EPI acquisitions to provide additional information in the characterization of maxillofacial bone lesions. Finally, figure 8 shows a case of an intraspinal epidural hematoma,

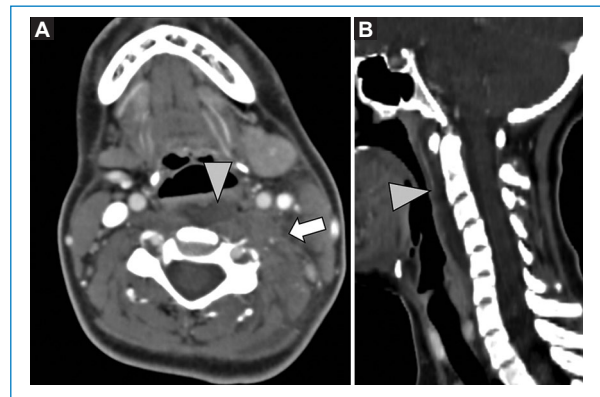


**Figure 5.** Contrast-enhanced computed tomography, axial (**A**) and sagittal (**B**). Left paravertebral inflammatory process (arrow) and increased volume of the retropharyngeal space (arrowhead). Purulent content and edema in the retropharyngeal space cannot be differentiated.

where the reduction of artifacts due to magnetic susceptibility allowed for a more precise assessment of the location and extent of the hematoma.

These examples reinforce the practical usefulness of non-EPI diffusion techniques in the evaluation of lesions in complex anatomical regions, where conventional EPI sequences often have diagnostic limitations.

### Impact on the clinical workflow

The incorporation of non-EPI techniques into protocols implies adjustments to the workflow of imaging departments. Although these sequences offer substantial improvements in image quality and a reduction of artifacts, they usually require longer acquisition times compared to conventional EPI, which may limit their

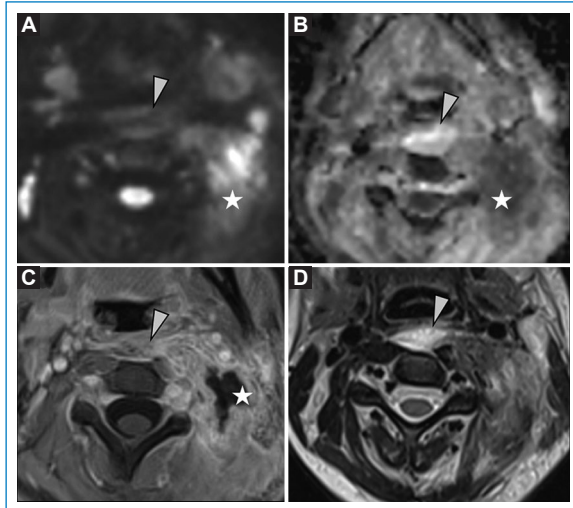


**Figure 6.** **A** and **B:** Siemens 1.5 T Axial RESOLVE diffusion. **C:** T1-weighted image after gadolinium. **D:** T2-weighted SE image. Left paravertebral lymphadenopathy, suppurative or abscessed with central purulent content, showing diffusion restriction and peripheral capsular enhancement (star). Retropharyngeal edema/phlegmon. Occupation of the retropharyngeal space by contents (arrowhead) with facilitated diffusion, mild enhancement, and high T2 signal. This avoided a surgical intervention of the retropharyngeal space.

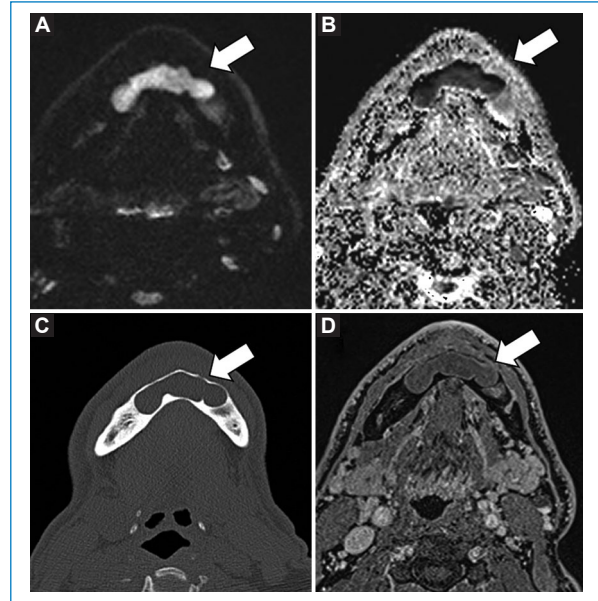


**Figure 7.** **A** and **B:** Siemens 1.5 T Axial RESOLVE diffusion. **C:** computed tomography with bone algorithm. **D:** T1-weighted image after gadolinium. Patient with Gorlin-Goltz syndrome. Mandibular keratocyst (arrow) showing intense diffusion restriction, expansive and lytic behavior on computed tomography, and absence of enhancement.

application in uncooperative patients or in high-demand healthcare settings.

From an operational perspective, it is essential that technical staff (medical technologists) be trained in the correct selection of the parameters (e.g., *b* values, OVS, artifact reduction strategies), as well as in identifying the specific limitations of each technique. Regarding interpretation, radiologists must familiarize themselves with the various available alternatives, understand their main characteristics, and know which ones are available on their MRI scanners in order to make the best choice according to the anatomical region to be studied.

In this context, the successful implementation of these techniques requires strategic planning that considers the availability of compatible hardware, ongoing training of the staff, and the selection of priority clinical indications where the diagnostic advantages justify their incorporation into routine practice.

## Conclusion

Recent advances in acquisition, compared to the standard SSH-EPI technique, have improved image fidelity,

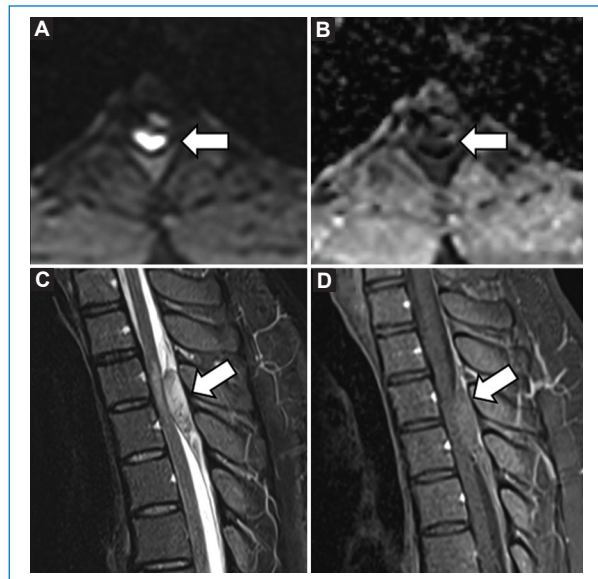


**Figure 8.** **A** and **B:** Siemens 1.5 T Axial RESOLVE diffusion. **C** and **D:** T1-weighted and T1-weighted sequences after gadolinium and with fat saturation, respectively. Posterior epidural intraspinal content (arrow) in the thoracic spine showing diffusion restriction, heterogeneous hyperintensity on T2, and absence of enhancement, consistent with a spontaneous epidural intraspinal hematoma with compressive myelopathy.

in some cases reducing scan times and optimizing the signal-to-noise ratio (SNR). Methods such as rs-EPI, HASTE DWI, rFOV, and PROPELLER DWI are already available in clinical practice to minimize distortions and improve diagnosis within reasonable timeframes.

The appropriate selection of the *b* values, along with choosing the most suitable acquisition technique based on the anatomical region and clinical objective, are fundamental to maximizing the diagnostic performance of DWI. Furthermore, implementing these sequences in clinical practice requires considering their impact on workflow, staff training, and hardware availability.

Taken together, these technical and operational considerations allow non-EPI sequences to become established as a robust and complementary alternative to conventional techniques, significantly expanding the applications of diffusion-weighted magnetic resonance imaging in the head, neck, and spinal cord.

## Funding

The authors declare that they have not received funding.

## Conflicts of interest

The authors declare no conflicts of interest.

## Ethical considerations

**Protection of human subjects and animal.** The authors declare that the procedures followed were in accordance with the ethical standards of the responsible committee on human experimentation and with the World Medical Association and the Declaration of Helsinki. The procedures were authorized by the Institutional Ethics Committee.

**Confidentiality, informed consent, and ethical approval.** The authors have obtained approval from the Ethics Committee for the analysis of routinely collected and anonymized clinical data; therefore, individual informed consent was not required. Relevant ethical recommendations have been followed.

**Declaration on the use of artificial intelligence.** The authors declare that no generative artificial intelligence was used in the writing or creation of the content of this manuscript.

## References

1. Le Bihan D, Lima M. Diffusion magnetic resonance imaging: what water tells us about biological tissues. *PLoS Biol.* 2015;13:e1002203.

2. Boucher F, Liao E, Srinivasan A. Diffusion-weighted imaging of the head and neck (including temporal bone). *Magn Reson Imaging Clin N Am.* 2021;29:205-32.
3. Le Bihan D, Poupon C, Amadon A, Lethimonnier F. Artifacts and pitfalls in diffusion MRI. *J Magn Reson Imaging.* 2006;24:478-88.
4. Tang L, Zhou XJ. Diffusion MRI of cancer: from low to high *b* values. *J Magn Reson Imaging.* 2019;49:23-40.
5. Norris CD, Quick SE, Parker JG, Koontz NA. Diffusion MR imaging in the head and neck. *Neuroimaging Clin N Am.* 2020;30:261-82.
6. Wilm BJ, Svensson J, Henning A, Pruessmann KP, Boesiger P, Kollias SS. Reduced field-of-view MRI using outer volume suppression for spinal cord diffusion imaging. *Magn Reson Med.* 2007;57:625-30.
7. Bihan D Le, Turner R, Macfall JR. Effects of intravoxel incoherent motions (IVIM) in steady-state free precession (SSFP) imaging: application to molecular diffusion imaging. *Magn Reson Med.* 1989;10:324-37.
8. de Bondt RBJ, Hoeberigs MC, Nelemans PJ, Deserno WMLLG, Peutz-Kootstra C, Kremer B, et al. Diagnostic accuracy and additional value of diffusion-weighted imaging for discrimination of malignant cervical lymph nodes in head and neck squamous cell carcinoma. *Neuroradiology.* 2009;51:183-92.
9. Abdel Razek A, Mossad A, Ghonim M. Role of diffusion-weighted MR imaging in assessing malignant versus benign skull-base lesions. *Radiol Med.* 2011;116:125-32.
10. Wu W, Miller KL. Image formation in diffusion MRI: a review of recent technical developments. *J Magn Reson Imaging.* 2017;46:646-62.
11. Bammer R, Auer M, Keeling SL, Augustin M, Stables LA, Prokesch RW, et al. Diffusion tensor imaging using single-shot SENSE-EPI. *Magn Reson Med.* 2002;48:128-36.
12. Ikeda H, Ohno Y, Murayama K, Yamamoto K, Iwase A, Fukuba T, et al. Compressed sensing and parallel imaging accelerated T2 FSE sequence for head and neck MR imaging: comparison of its utility in routine clinical practice. *Eur J Radiol.* 202;135:109501.
13. Yoshida N, Nakaura T, Morita K, Yoneyama M, Tanoue S, Yokota Y, et al. Echo planar imaging with compressed sensitivity encoding (EPICS): usefulness for head and neck diffusion-weighted MRI. *Eur J Radiol.* 2022;155:110489.
14. Robson MD, Anderson AW, Gore JC. Diffusion-weighted multiple shot echo planar imaging of humans without navigation. *Magn Reson Med.* 1997;38:82-8.
15. Porter DA, Heidemann RM. High resolution diffusion-weighted imaging using readout-segmented echo-planar imaging, parallel imaging and a two-dimensional navigator-based reacquisition. *Magn Reson Med.* 2009;62:468-75.
16. Holdsworth SJ, Skare S, Newbould RD, Guzman R, Blevins NH, Bammer R. Readout-segmented EPI for rapid high resolution diffusion imaging at 3T. *Eur J Radiol.* 2008;65:36-46.
17. Constable RT, Gore JC. The loss of small objects in variable TE imaging: implications for FSE, RARE, and EPI. *Magn Reson Med.* 1992;28:9-24.
18. Sakamoto J, Sasaki Y, Otonari-Yamamoto M, Nishikawa K, Sano T. Diffusion-weighted imaging of the head and neck with HASTE: influence of imaging parameters on image quality. *Oral Radiol.* 2012;28:87-94.
19. Hennig J, Nauerth A, Friedburg H. RARE imaging: a fast imaging method for clinical MR. *Magn Reson Med.* 1986;3:823-33.
20. Kim TH, Baek MY, Park JE, Ryu YJ, Cheon JE, Kim IO, et al. Comparison of DWI methods in the pediatric brain: PROPELLER turbo spin-echo imaging versus readout-segmented echo-planar imaging versus single-shot echo-planar imaging. *Am J Roentgenol.* 2018;210:1352-8.
21. Feinberg DA, Hoenninger JC, Crooks LE, Kaufman L, Watts JC, Arakawa M. Inner volume MR imaging: technical concepts and their application. *Radiology.* 1985;156:743-7.
22. Wilm BJ, Svensson J, Henning A, Pruessmann KP, Boesiger P, Kollias SS. Reduced field-of-view MRI using outer volume suppression for spinal cord diffusion imaging. *Magn Reson Med.* 2007;57:625-30.
23. Rieseberg S, Frahm J, Finsterbusch J. Two-dimensional spatially-selective RF excitation pulses in echo-planar imaging. *Magn Reson Med.* 2002;47:1186-93.
24. Sharma M, Gupta A, Jana M, Kashyap S, Bakhshi S, Sharma S. Comparison of HASTE versus EPI-based DWI for retinoblastoma and correlation with prognostic histopathologic parameters. *Am J Neuroradiol.* 2024;45:198-204.
25. Bozer A, Adibelli ZH, Yener Y, Dalgıç A. Diagnostic performance of multi-shot echo-planar imaging (RESOLVE) and non-echo-planar imaging (HASTE) diffusion-weighted imaging in cholesteatoma with an emphasis on signal intensity ratio measurement. *Diagn Interv Radiol.* 2024;30:370-7.
26. Li Z, Pipe JG, Lee C, Debbins JP, Karis JP, Huo D. X-PROP: a fast and robust diffusion-weighted propeller technique. *Magn Reson Med.* 2011;66:341-7.
27. Shi J, Lin J, Zhou X, Yin N, Wu L, Yu M, et al. Comparison of reduced and full field of view in diffusion-weighted MRI on image quality: a meta-analysis. *J Magn Reson Imaging.* 2024;61:690-701.

## Pedunculated focal nodular hyperplasia complicated by torsion: a very rare atypical presentation

### Hiperplasia nodular focal pediculada complicada por una torsión: una presentación atípica muy rara

Yeison R. Gómez-Ledesma<sup>1\*</sup>, Catalina Cuervo-Valencia<sup>2</sup>, Catalina Posada-Cuartas<sup>3</sup>, Sergio Hoyos<sup>4,5</sup>, and Andrés F. Latorre-Pinto<sup>1</sup>

<sup>1</sup>Faculty of Medicine, Universidad CES; <sup>2</sup>Department of Radiology, Hospital Pablo Tobón Uribe; <sup>3</sup>Department of Radiology, Prodiagnóstico; <sup>4</sup>Hepatobiliary Surgery and Liver Transplant Unit, Hospital Pablo Tobón Uribe; <sup>5</sup>Gastrohepatology Group, Universidad de Antioquia. Medellín, Colombia

#### Abstract

Focal nodular hyperplasia (FNH) is a benign hepatic tumor that arises as a response to a probable vascular anomaly. It consists of a reactive hyperplastic growth of normal hepatocytes, a central scar with radial layout containing portal tracts and abnormal blood vessels, surrounded by normal hepatic parenchyma. It accounts for up to 8% of all primary hepatic tumors, being the second most common among benign neoplasms. It is more frequent in women, with intrahepatic localization in the right lobe and usually asymptomatic. Pedunculated FNH is the rarest atypical form of FNH, located in the extrahepatic region and connected to the liver by a pedicle. It is more commonly associated with symptoms and complications, thus surgical management is indicated. We report the case of a 19-year-old female patient presenting with a pedunculated FNH with torsion of the pedicle, requiring surgical management, with satisfactory postoperative evolution.

**Keywords:** Focal nodular hyperplasia. Pedunculated liver tumor. Liver neoplasms.

#### Resumen

La hiperplasia nodular focal (HNF) es un tumor hepático benigno que se presenta como respuesta a una probable anomalía vascular. Consiste en un crecimiento hiperplásico reactivo de hepatocitos normales, una cicatriz central de configuración radial con tractos portales y vasos sanguíneos anormales, y rodeado por parénquima hepático normal. Representa hasta un 8% de todos los tumores hepáticos primarios, siendo la segunda más frecuente de las neoplasias benignas. Es más habitual en las mujeres, con localización intrahepática en el lóbulo derecho y asintomática. La HNF pediculada es la forma atípica más rara de HNF, localizada en la región extrahepática y conectada al hígado por un pedículo. Se asocia con mayor frecuencia a síntomas y complicaciones, por lo cual está indicado el manejo quirúrgico. Reportamos el caso de una paciente de 19 años que presentó una HNF pediculada con torsión del pedículo, requiriendo manejo quirúrgico, y tuvo una adecuada evolución posoperatoria.

**Palabras clave:** Hiperplasia nodular focal. Tumor hepático pediculado. Neoplasias hepáticas.

#### \*Correspondence:

Yeison R. Gómez-Ledesma  
E-mail: gomezl.yeison@uces.edu.co

Date of reception: 01-02-2025

Date of acceptance: 18-05-2025

DOI: 10.24875/AJI.25000008

Available online: 28-04-2026

Austral J. Imaging. (Engl. ed.). 2026;32(2):89-92

[www.resochradi.com](http://www.resochradi.com)

2810-708X / © 2025 Sociedad Chilena de Radiología. Published by Permanyer. This is an open access article under the CC BY-NC-ND license (<https://creativecommons.org/licenses/by-nc-nd/4.0/>).

## Introduction

Focal nodular hyperplasia (FNH) is a benign liver tumor that arises as a response to a vascular abnormality. It is characterized by a central radial scar with portal tracts and anomalous blood vessels on a surrounding normal liver parenchyma. It is more frequent in women and is typically located intrahepatically in the right lobe. In 20% of cases, FNH is located outside the liver parenchyma, and of these, up to 9% present a pedunculated form, which is more frequently associated with symptoms and complications. Pedunculated FNH is the rarest form of FNH, with only 12 cases reported in the medical literature to date. It is characterized by its extrahepatic location, connected to the liver by a thin stalk (peduncle), and is more frequently associated with complications, thus requiring surgical treatment.

We report the case of a 19-year-old patient who presented with a pedunculated FNH complicated by a torsion of the peduncle, requiring surgical treatment, and had a satisfactory postoperative evolution.

## Case report

A 19-year-old woman with no prior medical history presented with a one-year history of a painless, mobile mass in the hypogastrium. An abdominal computed tomography (CT) scan with intravenous contrast was performed, revealing a pedunculated hypervascular mass originating from the hepatic segment III and extending to the pelvis (Fig. 1).

To characterize the lesion, an abdominal magnetic resonance imaging (MRI) scan with intravenous gadolinium contrast was performed (Fig. 2), establishing the radiological diagnosis of a pedunculated FNH, and the patient was scheduled for surgery.

While awaiting surgery, the patient was admitted to the emergency department after 24 hours of colicky pain, rated 7/10 in intensity, in the right flank and iliac fossa, associated with progressive abdominal distension, nausea, and vomiting. The patient was hospitalized, and over the following hours, the abdominal pain increased in intensity, accompanied by hypotension. Physical examination revealed no signs of peritoneal irritation suggestive of acute appendicitis or any other cause of acute abdomen. She was evaluated by the hepatobiliary surgery service, where recent imaging studies were reassessed, and torsion of the lesion was suspected. Therefore, it was decided to perform urgent

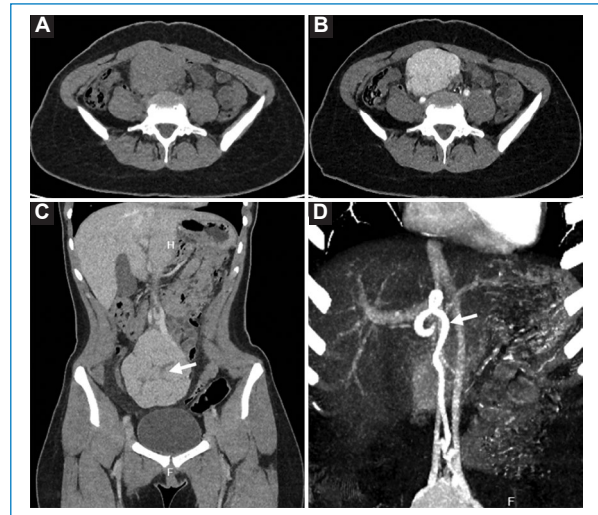


**Figure 1.** Abdominal computed tomography images with intravenous iodinated contrast showing a lobulated mass with a peduncle originating from hepatic segment III, extending into the pelvis, which is isodense to the liver in the simple (non-contrast) phase (A), with homogeneous avid enhancement in the arterial phase (B) and isodense in the portal phase (C), with a hypodense center of radial configuration that corresponds to a central scar (arrow in C). In the arterial phase with maximum intensity projection and coronal reconstruction (D), an ectatic and tortuous artery is observed (arrow) originating from the left hepatic artery, which is hypertrophic and supplies blood to the mass.

laparoscopic surgery, during which a pedunculated mass measuring 10 × 9 × 6 cm was removed (Fig. 3).

The patient had a good postoperative evolution and was discharged the following day without subsequent complications.

The pathology report informed a centrally located mass with multiple fibrous scars, corresponding to a FNH with vascular ectasia and peduncle congestion due to torsion.

## Discussion

FNH has an incidence of 0.9%, it is more frequent in women (80-90%) and is usually diagnosed between the third and fifth decades of life<sup>1-4</sup>.

Pedunculated FNH is the rarest atypical form, located in the extrahepatic region and connected to the liver by a thin stalk or peduncle<sup>5-8</sup>. The characteristics that classify it as atypical, in this case, are its exophytic presentation and size, since the dynamic behavior with contrast corresponds to typical radiological findings.

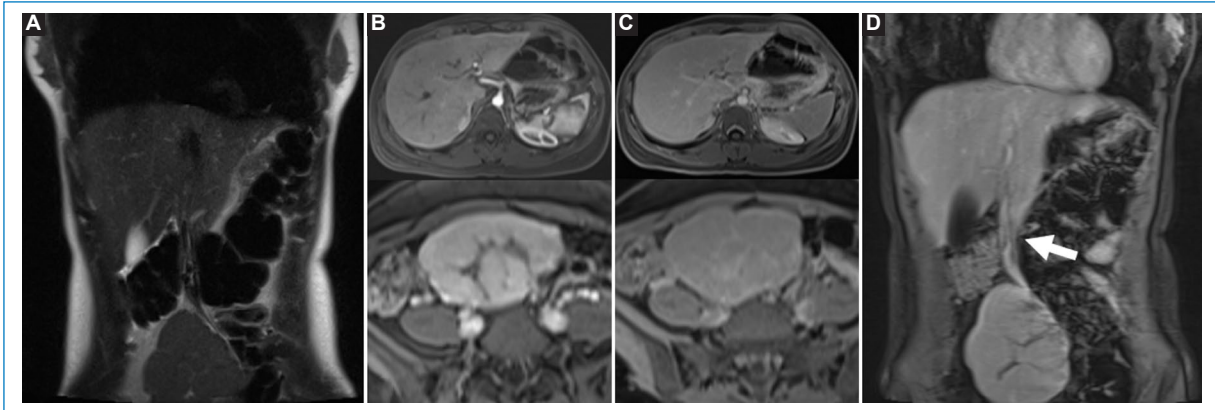


**Figure 2.** Abdominal magnetic resonance imaging with intravenous extracellular (gadolinium) contrast. The lesion is isointense to the liver on pre-contrast T1 and T2 sequences, with a center corresponding to the central scar, showing intermediate-to-high signal intensity on T2 sequences (A) and mildly hypointense on T1. In the dynamic post-contrast phases, it shows homogeneous avid enhancement in the arterial phase (B) and isointense in the portal and delayed phases (D and C, respectively). The central scar is hypointense in the early phases with enhancement in the delayed post-contrast phase (D), where the vascular pedicle can be seen (arrow).

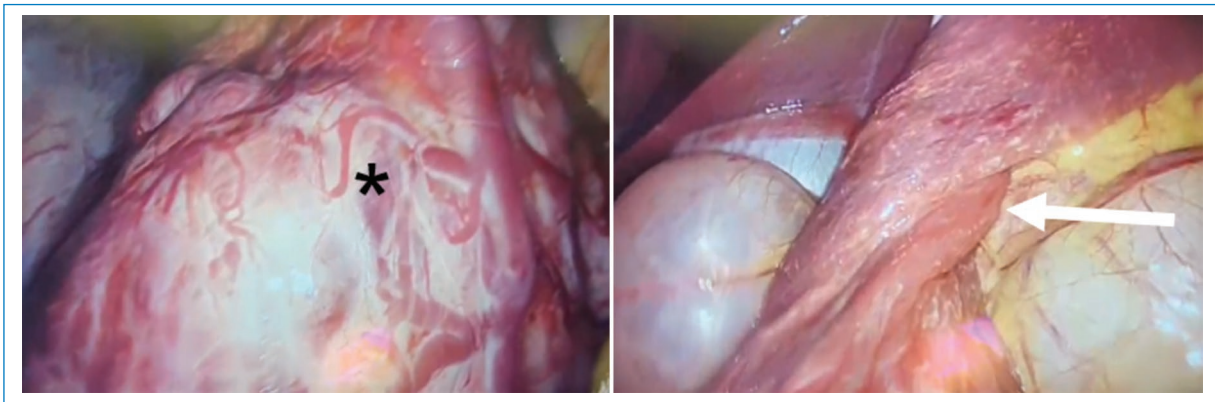


**Figure 3.** Photographs taken during laparoscopic surgery showing a large hypervascular mass (asterisk) with a thick peduncle (arrow), originating from the left hepatic lobe and exhibiting 180° torsion.

Pedunculated FNH is more likely to be symptomatic, with pain generally located in the epigastrium and right hypochondrium, which may be secondary to a mass effect with compression of surrounding vessels, gastric outlet obstruction, hemorrhage, and torsion of the peduncle with infarction of the tumor<sup>8,9</sup>. Compression of the hepatic artery and portal vein at the hepatic hilum has been reported, with thrombosis of the extrahepatic portal vein<sup>2,8</sup>. Gastric outlet obstruction has been associated with pedunculated lesions originating from segments II, III, IV, and V<sup>5</sup>. Hemorrhage may be secondary to the rupture of vessels located in the stalk of the lesion<sup>5,6</sup>. Torsion of the peduncle can lead to infarction

of the tumor and sudden onset or worsening of abdominal pain<sup>5,6</sup>, as in our case, since the patient presented with acute abdominal pain.

Radiologically, the FNH correlates well with the histological findings, and its characteristics are similar across all imaging techniques. Generally, it is a single, well-defined, lobulated mass without a capsule, measuring less than 5 cm, and is similar to the parenchyma on pre-intravenous contrast images. On post-contrast images, it shows avid and homogeneous enhancement in the arterial phase, and subtle or iso-enhancement in the portal and delayed phases, presenting a central scar that only enhances in the delayed phases<sup>5,7,10</sup>.

Hepatic tumors with a pedunculated exophytic component tend to be very rare, and when present, the peduncle is usually not visible on imaging techniques. The imaging characteristics of these tumors are similar to those of intrahepatic lesions, except for their location<sup>5-7</sup>.

Surgical treatment has been proposed for patients with atypical symptoms, complications, and presentations with an exophytic component, and when there is diagnostic uncertainty<sup>7-10</sup>. In this patient, scheduled surgical treatment was proposed due to the atypical presentation, symptoms, and potential risk of complications. While awaiting surgery, the patient developed acute abdominal pain secondary to torsion of the lesion and required urgent surgery.

In the cases of pedunculated FNH reported in the literature, surgical resection was chosen due to the higher risk of complications and for histological confirmation, given its atypical presentation. The surgical resection has been performed laparoscopically, which is less invasive and, due to the morphological characteristics of pedunculated growth, allows for successful resection, as in our case. Another treatment option that has been described is embolization of the lesion's feeding vessels<sup>8-10</sup>.

Hepatic tumors with an exophytic pattern should be considered in the differential diagnosis, including hepatic hemangioma, hepatocellular adenoma, angiolipoma, solitary fibrous tumor, hepatocellular carcinoma, cholangiocarcinoma, lymphatic malformations, and metastases<sup>9,10</sup>.

## Conclusions

Pedunculated FNH is a very rare and difficult-to-diagnose primary benign hepatic neoplasm, as it can be confused with other types of benign or malignant tumors. It carries a higher risk of complications than the typical form and, therefore, requires surgical resection to establish a definitive diagnosis and to avoid complications.

## Funding

The authors declare that they have not received funding.

## Conflicts of interest

The authors declare no conflicts of interest.

## Ethical considerations

**Protection of human subjects and animals.** The authors declare that the procedures followed were in accordance with the ethical standards of the responsible committee on human experimentation and with the World Medical Association and the Declaration of Helsinki. The procedures were authorized by the Institutional Ethics Committee.

**Confidentiality, informed consent, and ethical approval.** The authors have followed their institution's confidentiality protocols, obtained informed consent from the patient, and secured approval from the Ethics Committee. SAGER guidelines have been followed as applicable to the nature of the study.

**Declaration on the use of artificial intelligence.** The authors declare that no generative artificial intelligence was used in the writing or creation of the content of this manuscript.

## References

1. Tsukui M, Morimoto N, Murayama K, Otake T, Watanabe S, Ishikawa T, et al. A case of pedunculated focal nodular hyperplasia treated by laparoscopic hepatectomy. *J Dig Dis Hepatol.* 2017;1: JDDH-134.
2. Khan MR, Saleem T, Haq TU, Aftab K. Atypical focal nodular hyperplasia of the liver. *Hepatobiliary Pancreat Dis Int.* 2011;10: 104-6.
3. Martiniuc A, Dumitracu T. Pedunculated focal nodular hyperplasia of the liver. *Surg Gastroenterol Oncol.* 2018;23:79-82.
4. LeGout JD, Bolan CW, Bowman AW, Caserta MP, Chen FK, Cox KL, et al. Focal nodular hyperplasia and focal nodular hyperplasia-like lesions. *Radiographics.* 2022;42:1043-61.
5. Ben Ismail I, Zenaidi H, Jouini R, Rebi S, Zoghli A. Pedunculated hepatic focal nodular hyperplasia: a case report and review of the literature. *Clin Case Rep.* 2021;9:1-4.
6. Zeina AR, Glick Y. Pedunculated hepatic focal nodular hyperplasia. *Ann Hepatol.* 2016;15:929-31.
7. Badea R, Meszaros M, Al Hajjar N, Rusu I, Chiorean L. Benign nodular hyperplasia of the liver-pedunculated form: diagnostic contributions of ultrasonography and consideration of exophytic liver tumors. *J Med Ultrason.* 2015;42:97-102.
8. Nandy K, Patkar S, Goel M. Massive pedunculated focal nodular hyperplasia: a diagnostic dilemma. *J Gastrointest Surg.* 2023;27: 1746-8.
9. Foutziti S, Giatromanolaki A, Chrysafis I, Deftereos SP. Is there any special imaging finding in a pedunculated focal nodular hyperplasia with suspected torsion? *Radiol Case Rep.* 2022;13: 243-5.
10. Koolwal J, Birkemeier KL, Zreik RT, Mattix KD. Pedunculated focal nodular hyperplasia in a healthy toddler. *Baylor Univ Med Cent Proc.* 2018;31:97-9.

## Anomalous pulmonary venous drainage, mixed type: report of an uncommon case

### *Drenaje venoso pulmonar anómalo, modalidad mixta: reporte de un caso poco común*

Fernando A. Mijangos-Vergara, Iván Turriza-Sosa, Patricia B. Bolado-García\*, and Naomi Solis-Tun

Diagnostic and Therapeutic Imaging Service, Unidad Médica de Alta Especialidad (UMAE), Hospital de Especialidades Centro Médico Nacional Ignacio García Téllez, Instituto Mexicano del Seguro Social, Merida, Yucatan, Mexico

#### Abstract

Anomalous pulmonary venous drainage (APVD) is a rare congenital anomaly in which the pulmonary veins do not connect normally to the left atrium. Mixed-modality APVD is particularly rare and therefore represents a diagnostic and therapeutic challenge. In this article, we report a case of mixed-modality APVD in a 9-month-old female patient, who initially presented with progressive respiratory distress and was subsequently diagnosed with APVD at a high-complexity healthcare center, by means of computed tomography angiography. The purpose of the publication is to document and share details that may help other medical professionals recognize and diagnose similar cases in the future.

**Keywords:** Congenital heart disease. Computed tomography angiography. Diagnostic imaging. Anomalous venous drainage.

#### Resumen

El drenaje venoso pulmonar anómalo (DVPA) es una rara anomalía congénita en la que las venas pulmonares no se conectan normalmente a la aurícula izquierda. La modalidad mixta de DVPA es particularmente infrecuente y por lo tanto representa un desafío diagnóstico y terapéutico. En este artículo se reporta un caso de DVPA de modalidad mixta, en paciente de sexo femenino de 9 meses de edad, quien presentó inicialmente un cuadro de dificultad respiratoria progresiva y posteriormente fue diagnosticada con DVPA en un centro médico de alta complejidad, mediante angiotomografía. El propósito de la publicación es documentar y compartir detalles que pueden ayudar a otros profesionales médicos a reconocer y diagnosticar casos similares en el futuro.

**Palabras clave:** Cardiopatía congénita. Angiotomografía. Diagnóstico por imagen. Drenaje venoso anómalo.

#### \*Correspondence:

Patricia B. Bolado-García  
E-mail: patricia.bolado@imss.gob.mx

Date of reception: 22-11-2024  
Date of acceptance: 18-05-2025  
DOI: 10.24875/AJI.24000060

Available online: 28-04-2026  
Austral J. Imaging. (Engl. ed.). 2026;32(2):93-97  
[www.resochradi.com](http://www.resochradi.com)

2810-708X / © 2025 Sociedad Chilena de Radiología. Published by Permanyer. This is an open access article under the CC BY-NC-ND license (<https://creativecommons.org/licenses/by-nc-nd/4.0/>).

## Introduction

Anomalous pulmonary venous drainage (APVD) is the drainage of one or more pulmonary veins outside the left atrium; it can generally be classified into two types, partial or total. Its detection is critical due to its strong association with other congenital heart defects, as well as with cardiac and respiratory anomalies, which have significant implications for the treatment of each patient. Knowledge of these abnormalities is vital, since the imaging specialist is often the first person to make such a diagnosis. Diagnosis can be difficult, go unnoticed, or only be made at late clinical presentation in adulthood.

Advances in non-invasive imaging have refined the radiological evaluation. Electrocardiogram-triggered cardiac computed tomography allows for a detailed anatomical evaluation with an excellent resolution, while cardiac magnetic resonance imaging allows for the assessment of anatomy, physiology, ventricular function, and volumetry. Techniques such as echocardiography and chest radiography should be considered complementary<sup>1</sup>.

In this unit, thoracic computed tomography angiography (CTA) is the confirmatory method for complex cases of congenital heart disease visualized by echocardiography.

## Clinical case

This is a 9-month-old patient with no significant family history. Her prenatal history includes a normal pregnancy, delivery via repeated cesarean section, a normal birth weight, and discharged without apparent complications. She begins with respiratory distress of 20 days' duration, showing progressive deterioration. Initially treated as an apparent infectious condition; however, due to lack of improvement, further studies are requested, including a chest X-ray, which reveals grade III cardiomegaly, primarily affecting the right heart chambers (Fig. 1). On physical examination, a murmur was identified. Given the clinical and imaging findings, a pediatric cardiology consultation was requested, who performed a transthoracic echocardiogram, where it was reported: *situs solitus*, levocardia with levoapex, concordant atrioventricular and ventricle-arterial connection, anomalous drainage of three pulmonary veins was observed: right and left superior and right inferior, reaching a collector that empties into the brachiocephalic (or innominate) vein, which in turn reaches the superior vena cava and the left inferior pulmonary vein, reaching the portal vein, with dilated suprahepatic veins

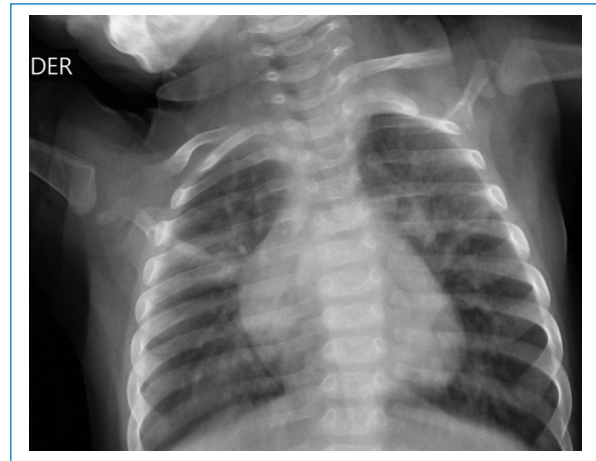


**Figure 1.** Chest X-ray in anteroposterior projection showing increased cardiac dimensions at the expense of the right chambers.

independently reaching the right atrium, the right atrium is observed to be dilated, with an interatrial septal defect, the left atrium is observed to be hypoplastic. Given the complexity of the findings, and after obtaining informed consent, anesthetic evaluation, and renal function tests (which were normal), a thoracic CT angiography was performed under sedation using the unit's equipment (Toshiba Aquilion 64-slice CT scanner) with administration of water-soluble, non-ionic iodinated contrast at a concentration of 350 mg/ml, at an injection rate of 2 ml/s, with SureStar at a threshold of 80 HU, performing multiparametric and three-dimensional reconstructions. Identified in said CT angiography was: *situs solitus*, levocardia with levoapex, concordant atrioventricular and ventricle-arterial connection, there is increased caliber of the right heart chambers, and decreased volume of the left heart chambers.

Regarding the assessment of the pulmonary veins, it was observed that the right superior and inferior pulmonary veins, as well as the left superior pulmonary vein, joined a collector vein and drained via a vertical vein into the brachiocephalic vein (Fig. 2), which causes an increase in the caliber of both this and the superior vena cava.

An infracardiac connection was observed between the left inferior pulmonary vein and the portal vein, which also showed increased caliber (Fig. 3).

A 3D reconstruction was performed to improve the characterization of the findings (Fig. 4).

Other findings reported: a 9 mm interatrial defect, not shown in the images obtained. No other relevant alterations were found in the thoracic assessment.

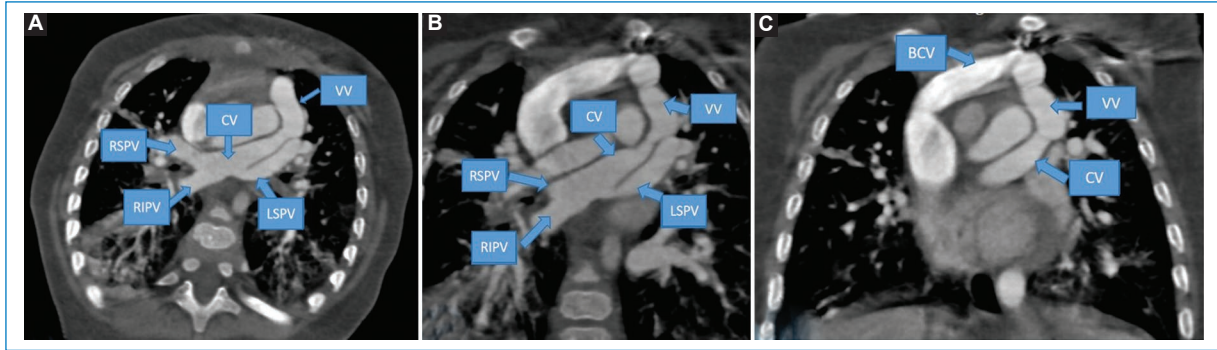


**Figure 2.** **A:** magnification of a thoracic CT angiogram in an oblique axial slice, the bone window where it is possible to visualize common drainage of the right superior pulmonary vein (RSPV), right inferior pulmonary vein (RIPV), and left superior pulmonary vein (LSPV) into the collector vein (CV), which communicates with the vertical vein (VV), which drains into the brachiocephalic vein (BCV), as can be seen in **B** and **C**, which correspond to magnifications of a thoracic CT angiogram in an oblique coronal slice (*source: WebDiagRX institutional electronic storage system*).

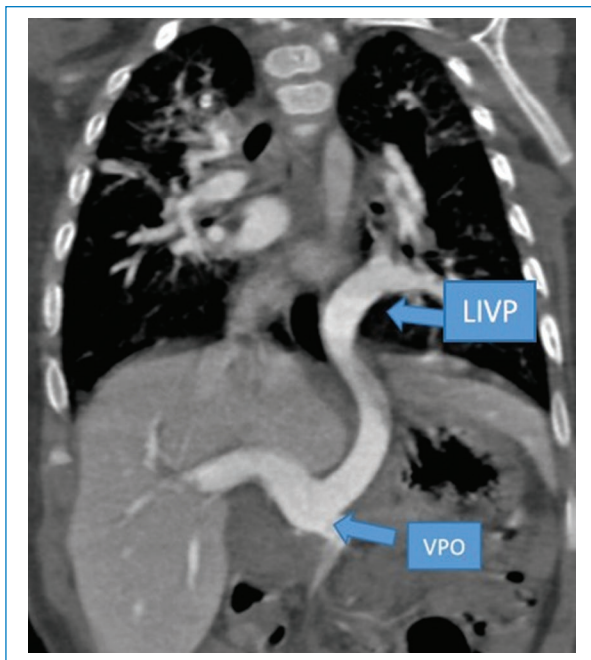


**Figure 3.** Magnification of a thoracic CT angiogram in an oblique coronal slice, mediastinal window where it is possible to visualize the drainage of the left inferior pulmonary vein (LIPV) into the portal vein (VPO), the same that appears with its caliber increased (*source: WebDiagRX institutional electronic storage system*).

## Discussion

The typical arrangement of normal pulmonary venous anatomy consists of four separate pulmonary veins: right superior and inferior pulmonary veins and left superior and inferior pulmonary veins, which drain individually into the left atrium, as depicted in [figure 5](#)<sup>1</sup>.

Lung development begins at approximately 26 days of gestation with the formation of the respiratory diverticulum, the associated venous plexus communicates with the systemic cardinal and umbilical veins, thus forming the initial pathway for pulmonary venous drainage. At 27–29 days, an out-pouching develops from the posterosuperior wall of the primitive left atrium, this pouch begins to communicate with the pulmonary venous component; simultaneously, the systemic veins involute, thus separating the two venous systems. In normal embryos, complete separation of these venous systems occurs, resulting in four separate pulmonary veins that drain into the left atrium. Failure of this separation process leads to various types of anomalous venous drainage<sup>1</sup>.

The right superior pulmonary vein drains the right upper and middle lobes of the lung, and the right inferior pulmonary vein drains the right lower lobe. The left superior pulmonary vein drains the lingula and the left upper lobe, while the left lower lobe is drained by the left inferior pulmonary vein<sup>1</sup>. This anatomical arrangement is found in 60–70% of the population<sup>2</sup>.

There are several normal variants of pulmonary venous drainage, which are usually a common incidental finding. Normal variants often consist of conjoined or accessory veins<sup>3</sup>.

## Anomalous pulmonary venous drainage

Anomalous pulmonary venous drainage (APVD) is the drainage of one or more pulmonary veins outside the left atrium; it can generally be considered of two types: partial or total<sup>4</sup>.

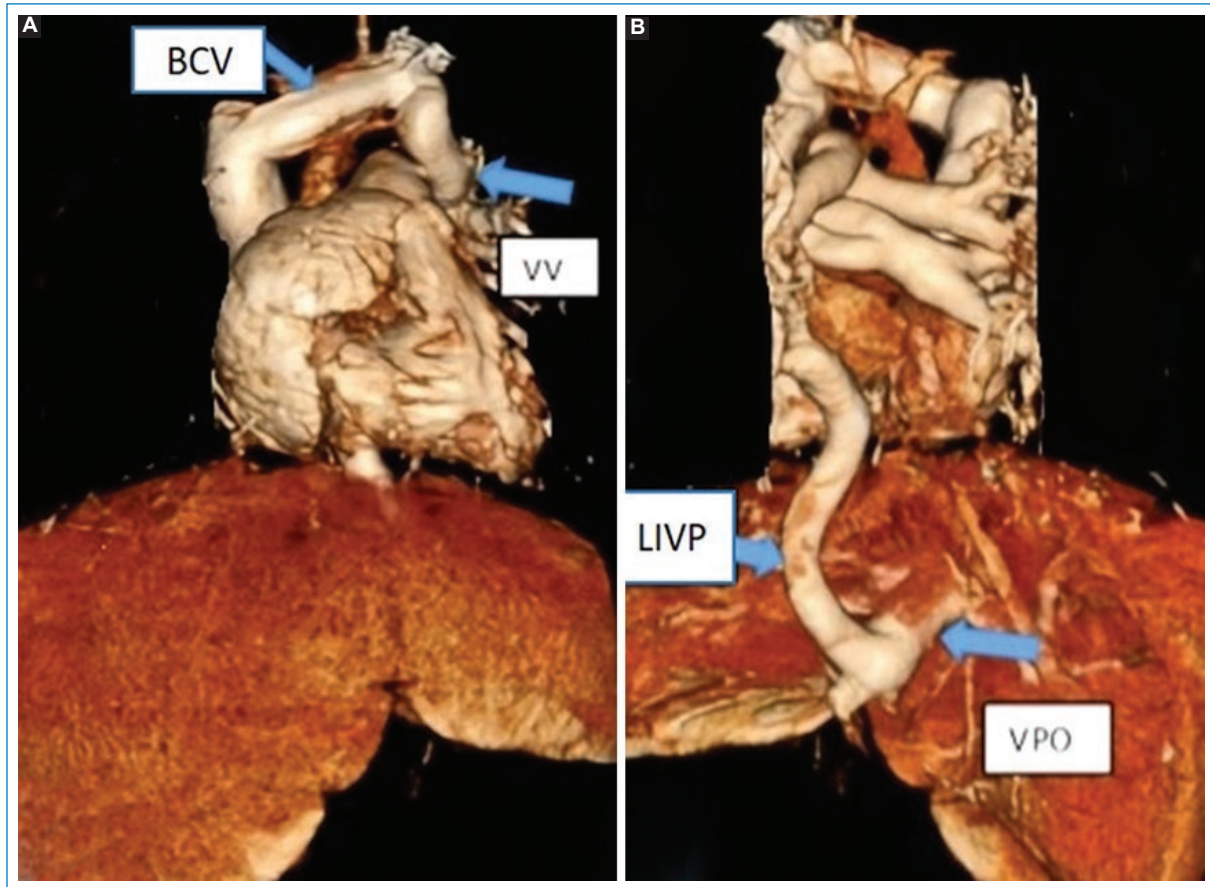


**Figure 4.** 3D thoracic CT angiography reconstructions. (source: WebDiagRX institutional electronic storage system). **A:** anterior view, **B:** posterior view. In **A**, the vertical vein (VV) draining into the brachiocephalic vein (BCV). **B:** the left inferior pulmonary vein (LIPV) draining into the portal vein (VPO).



**Figure 5.** Three-dimensional reconstruction of a CT angiogram depicting the normal anatomy of the pulmonary veins (adapted from Lyen et al.<sup>7</sup>). **1:** left superior pulmonary vein. **2:** left inferior pulmonary vein. **3:** right superior pulmonary vein. **4:** right inferior pulmonary vein.

The clinical presentation is variable, the symptom depends on whether there is pulmonary venous return obstruction at the vertical vein, restriction of the flow from the atrial septal defect, or both, with tachypnea being the most frequent symptom<sup>5</sup>.

Partial anomalous pulmonary venous drainage (PAPVD) describes the connection of at least one, but not all, pulmonary veins to the systemic venous system or to the right atrium. The prevalence of partial APVD has been reported to be between 0.4% and 0.7%<sup>4</sup>.

The most common form of partial APVD is anomalous drainage of the right superior pulmonary vein into the superior vena cava<sup>6</sup>.

Identifying these anomalies has a significant influence on surgical treatment, as the anomalous pulmonary veins may be redirected to the left atrium through an interatrial communication (atrial septal defects).

Total anomalous pulmonary venous drainage (TAPVD) refers to the drainage of all four pulmonary

veins into a cardiovascular structure other than the left atrium<sup>7</sup> and represents approximately 2% of cardiac malformations<sup>1</sup>.

There are four types, depending on the level of drainage:

- Type 1: supracardiac. This accounts for up to 55% of cases and is the most common. It typically involves the convergence of all four pulmonary veins behind the heart to form a common vein<sup>1</sup>. In this type, drainage most commonly occurs through a vertical vein into the left brachiocephalic vein. On rare occasions, the supracardiac total APVD may drain directly into a right superior vena cava, a left superior vena cava, or an azygos system<sup>8</sup>.
- Type 2: abnormal communication at the cardiac level. The drainage occurs into the right atrium or the coronary sinus<sup>1</sup>. This accounts for approximately 21% of cases<sup>9</sup>.
- Type 3: drainage below the level of the heart or diaphragm, for example, into the inferior vena cava, portal vein, or hepatic vein<sup>1</sup>. This accounts for approximately 26% of cases<sup>9</sup>.
- Type 4: drainage at more than one level, a mixed type. The pulmonary veins drain to at least two different locations, including the brachiocephalic vein, superior vena cava, azygos vein, coronary sinus, right atrium, or below the diaphragm. This type of APVD accounts for approximately 9% of cases, making it the least common<sup>9</sup>.

In patients with total APVD, a right-to-left shunt is crucial for early survival and this usually manifests as a patent foramen ovale or an interatrial communication (atrial septal defect). Patients present in the neonatal period with symptoms of congestive heart failure and cyanosis.

Prompt surgical repair is essential, which is why it is rarely seen on CT imaging or MRI scans.

In the vast majority of cases, echocardiography is the cornerstone of the diagnosis and anatomical description of total APVD, so cross-sectional images are reserved for when the diagnosis is unclear on echocardiography<sup>10</sup>.

## Conclusion

This report describes an uncommon case of mixed-type APVD, a rare and complex condition that presents significant diagnostic and therapeutic challenges. Accurate identification of this anomaly is crucial for appropriate patient treatment, as it directly influences surgical decisions and long-term prognosis. This case underscores the importance of a multidisciplinary approach and the use of advanced imaging techniques for diagnosis

and treatment planning. The documentation and study of rare cases such as this one contributes to improving the knowledge and understanding of anatomical variations and their clinical implications, helping to optimize outcomes for future patients with similar conditions.

## Funding

The authors declare that they have not received funding.

## Conflicts of interest

The authors declare no conflicts of interest.

## Ethical considerations

**Protection of human subjects and animals.** The authors declare that no experiments on humans or animals were performed for this research.

**Confidentiality, informed consent, and ethical approval.** The authors have followed their institution's confidentiality protocols, obtained informed consent from the patient's parents, and secured approval from the Ethics Committee. SAGER guidelines have been followed as applicable to the nature of the study.

**Declaration on the use of artificial intelligence.** The authors declare that no generative artificial intelligence was used in the writing or creation of the content of this manuscript.

## References

1. Lyen S, Wijesuriya S, Ngan-Soo E, Mathias H, Yeong M, Hamilton M, et al. Anomalous pulmonary venous drainage: a pictorial essay with a CT focus. *Journal of Congenital Cardiology*. 2017;1:1-3.
2. Ghaye B, Szapiro D, Dacher JN, Rodríguez LM, Timmermans C, Devillers D, et al. Percutaneous ablation for atrial fibrillation: the role of cross-sectional imaging. *Radiographics*. 2003;23(suppl\_1):S19-33.
3. Lacomis JM, Wigginton W, Fuhrman C, Schwartzman D, Armfield DR, Pealer KM. Multi-detector row CT of the left atrium and pulmonary veins before radio-frequency catheter ablation for atrial fibrillation. *Radiographics*. 2003;23(suppl\_1):S35-48.
4. Dillman JR, Yarram SG, Hernandez RJ. Imaging of pulmonary venous developmental anomalies. *American Journal of Roentgenology*. 2009;192(5):1272-85.
5. Aroca Á, Polo L, Bret M, López-Ortego P, González A, Villagrà F. Drenaje venoso pulmonar anómalo total. *Técnicas y resultados*. *Cir Cardio*. 2014;21(2):90-6.
6. Demos TC, Posniak HV, Pierce KL, Olson MC, Muscato M. Venous anomalies of the thorax. *American Journal of Roentgenology*. 2004;182(5):1139-50.
7. Ferguson EC, Krishnamurthy R, Oldham SA. Classic imaging signs of congenital cardiovascular abnormalities. *Radiographics*. 2007;27(5):1323-34.
8. White CS, Baffa JM, Haney PJ, Pace ME, Campbell AB. MR imaging of congenital anomalies of the thoracic veins. *Radiographics*. 1997;17(3):595-608.
9. Karamlou T, Gurofsky R, Al Sukhni E, Coles JG, Williams WG, Caldarone CA, et al. Factors associated with mortality and reoperation in 377 children with total anomalous pulmonary venous connection. *Circulation*. 2007;115(12):1591-8.
10. Vyas HV, Greenberg SB, Krishnamurthy R. MR imaging and CT evaluation of congenital pulmonary vein abnormalities in neonates and infants. *Radiographics*. 2012;32(1):87-98.

## A rare cause of basal ganglia and thalamic hyperintensities: infantile nephropathic cystinosis

### Una causa poco frecuente de hiperintensidades en los ganglios basales y el tálamo: cistinosis nefropática infantil

Nipun Rajgarhia\*, Pranjal Gupta, and Amit Bajpai

Department of Radiodiagnosis and Imaging, Armed Forces Medical College, Pune, Maharashtra, India

#### Abstract

A 2-year-old female was presented with a history of polyuria, failure to thrive, and seizure. On examination, she was found to be anemic with multiple dot-like crystals in both corneas and whole genome sequencing revealing pathogenic mutation in the CTNS gene. Magnetic resonance imaging (MRI) brain showed T2/fluid-attenuated inversion recovery hyperintensities in both basal ganglia and thalamic and also in the pons. The patient was diagnosed as a case of infantile nephropathic cystinosis, which is a rare autosomal recessive lysosomal storage disorder caused by intracellular cystine accumulation. These patients often present with renal symptoms. MRI brain shows cortical atrophy with white matter hyperintensities commonly. These patients have a 12-fold increased risk of having Chiari malformation. The role of imaging is to establish the various central nervous system manifestations of the disease and also to predict the development of complications in adults.

**Keywords:** Infantile. Nephropathic. Cystinosis. Basal ganglia. Thalamus. Polyuria.

#### Resumen

Una niña de 2 años fue presentada con antecedentes de poliuria, retraso del crecimiento y convulsiones. En la exploración, se observó que presentaba anemia con múltiples cristales en forma de puntos en ambas córneas, y la secuenciación del genoma completo reveló una mutación patógena en el gen CTNS. La resonancia magnética cerebral mostró hiperintensidades T2/FLAIR en ambos ganglios basales y talámicos, así como en el puente. Se diagnosticó a la paciente un caso de cistinosis nefropática infantil, un trastorno de almacenamiento lisosomal autosómico recesivo poco frecuente causado por la acumulación intracelular de cistina. Estos pacientes suelen presentar síntomas renales. La resonancia magnética cerebral muestra comúnmente atrofia cortical con hiperintensidades en la sustancia blanca. Estos pacientes tienen un riesgo 12 veces mayor de padecer malformación de Chiari. La función de las imágenes es establecer las diversas manifestaciones de la enfermedad en el SNC y también predecir el desarrollo de complicaciones en adultos.

**Palabras clave:** Infantil. Nefropático. Cistinosis. Ganglios basales. Tálamo. Poliuria.

#### \*Correspondence:

Nipun Rajgarhia  
E-mail: nipunrajgarhia@gmail.com

Date of reception: 24-02-2025

Date of acceptance: 03-08-2025

DOI: 10.24875/AJI.25000012

Available online: 28-04-2026

Austral J. Imaging. (Engl. ed.). 2026;32(2):98-100

[www.resochradi.com](http://www.resochradi.com)

2810-708X / © 2025 Sociedad Chilena de Radiología. Published by Permanyer. This is an open access article under the CC BY-NC-ND license (<https://creativecommons.org/licenses/by-nc-nd/4.0/>).

## Introduction

Infantile nephropathic cystinosis is the most common and severe form of cystinosis which is the most common cause of renal Fanconi syndrome in childhood and is a treatable lysosomal storage disease. There is defect in the transport protein, Cystinosin, which is encoded by the CTNS gene, on chromosome 17p13, which results in lysosomal accumulation of cystine, which forms crystals and causes progressive organ injury. Symptoms begin in early infancy in the form of impaired growth, polyuria and polydipsia and results in end-stage renal disease (ESRD) by the end of the first decade.

## Clinical history

A 2-year-old female presented to the pediatric department with a history of polyuria, failure to thrive, and an episode of generalized tonic-clonic seizure. On anthropometry, her length, weight, and head circumference were found to be below 3 percentile for her age group.

Further investigations revealed a normochromic, normocytic anemia and a creatinine of 1.1 mg/dL. Ophthalmoscopy revealed multiple dot-like crystals seen in bilateral corneas in the subepithelial region, which were suggestive of cystinosis. Whole exome sequencing revealed a pathogenic mutation in the CTNS gene.

## Imaging findings

- Magnetic resonance imaging (MRI) revealed T2/fluid-attenuated inversion recovery hyperintensities involving bilateral internal capsule, bilateral anterior/ventral anterior thalami (Figs. 1 A and B), body of corpus callosum, and subcortical white matter of bilateral frontoparietal lobes. The posterior limb of the internal capsule also appeared hyperintense on T1-weighted images.
- These hyperintensities were also seen to extend along the white matter tracts bilaterally in the basal ganglia region and were seen reaching till the pons involving the pontine tegmentum (Figs. 2 A and B).
- Generalized prominence of sulcal and cisternal spaces was seen in both cerebral hemispheres.

## Discussion

### Background

Infantile nephropathic cystinosis is a lysosomal storage disorder caused by intracellular cystine accumulation. It is a rare autosomal recessive disorder with an estimated incidence of 1 case/100,000-200,000 live births<sup>1</sup>.

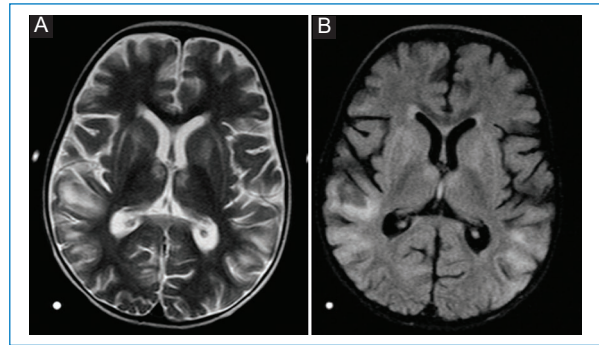


**Figure 1. A:** T2-weighted imaging axial showing hyperintensities involving bilateral anterior/ventral anterior thalami. **B:** fluid-attenuated inversion recovery axial showing hyperintensities involving bilateral anterior/ventral anterior thalami.

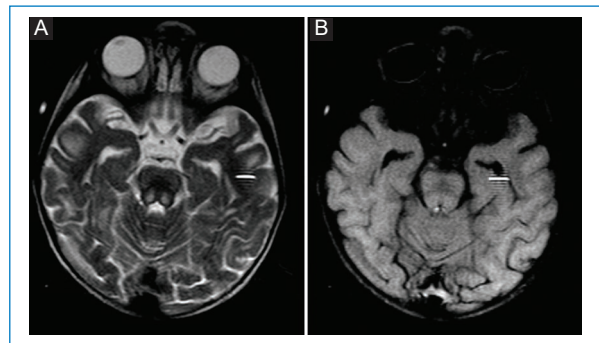


**Figure 2. A:** T2-weighted imaging axial showing hyperintensity involving the pontine tegmentum of the upper pons in the central tegmental tracts. **B:** fluid-attenuated inversion recovery axial showing hyperintensity involving the pontine tegmentum of the upper pons in the central tegmental tracts.

## Clinical perspective

- Renal symptoms predominate with features of polyuria, dehydration, and hypophosphatemic rickets
- Systemic involvement - photophobia, hypothyroidism, and a wide spectrum of central nervous system (CNS) manifestations such as myopathy, cerebral atrophy, seizures<sup>2</sup>.

### Imaging perspective: MRI

- A high prevalence of abnormalities on the brain scan has been seen, especially in adult patients<sup>3</sup>:
- Cortical atrophy - more in parieto-occipital regions.
- White matter hyperintensities

- Cerebral calcifications
- Others: These children are also shown to have a 12-fold risk of having Chiari malformations<sup>4</sup>.

## Outcome

This case emphasizes the role of radiological investigations, especially MRI, in establishing the various CNS manifestations of the disease and also in predicting the development of complications in adults.

## Take home message/Teaching points

In cases of infantile nephropathic cystinosis, the imaging findings in MRI can help in diagnosis as well as serve as a baseline for assessment of treatment response and progression of disease in adults. With the long-term survival of these patients steadily increasing due to effective dialysis and cysteamine therapy<sup>5</sup>, it is useful to have a knowledge of the spectrum of imaging manifestations.

## Final diagnosis

### Infantile nephropathic cystinosis

#### DIFFERENTIAL DIAGNOSIS LIST

- Mucopolysaccharidosis
- Hemolytic-Uremic syndrome
- Metachromatic leukodystrophy.

## Conclusion

Reaching an early diagnosis by leukocyte cystine assay/genetic sequencing along with prompt initiation of specific therapy with cysteamine, can effectively delay in the progression of renal failure.

## Funding

The authors declare that they have not received funding.

## Conflicts of interest

The authors declare no conflicts of interest.

## Ethical considerations

### Protection of human subjects and animals.

The authors declare that no experiments involving humans or animals were conducted for this research.

**Confidentiality, informed consent, and ethical approval.** The authors have followed their institution's confidentiality protocols, obtained informed consent from the patient's parents, and secured approval from the Ethics Committee. SAGER guidelines have been followed as applicable to the nature of the study.

### Declaration on the use of artificial intelligence.

The authors declare that no generative artificial intelligence was used in the writing or creation of the content of this manuscript.

## References

1. Gahl WA, Thoene JG, Schneider JA. Cystinosis. *N Engl J Med.* 2002;347:111-21.
2. Curie A, Touil N, Gaillard S, Galanaud D, Leboucq N, Deschenes G, et al. Neuropsychological and neuroanatomical phenotype in 17 patients with cystinosis. *Orphanet J Rare Dis.* 2020;15:59.
3. Servais A, Boigontier J, Saitovitch A, Hummel A, Boddaert N. Central nervous system complications in cystinosis: the role of neuroimaging. *Cells.* 2022;11:682.
4. Rao KI, Hesselink J, Trauner DA. Chiari I malformation in nephropathic cystinosis. *J Pediatr.* 2015;167:1126-9.
5. Brodin-Sartorius A, Tête MJ, Niaudet P, Antignac C, Guest G, Ottolenghi C, et al. Cysteamine therapy delays the progression of nephropathic cystinosis in late adolescents and adults. *Kidney Int.* 2012;81:179-89.